NEUROPHYSIOLOGY

Crossing nerve transfer drives sensory input–dependent plasticity for motor recovery after brain injury

Zhengrun Gao[1]†, Zhen Pang[1]†, Gaowei Lei[1]†, Yiming Chen[1]†, Zeyu Cai[1], Shuai Zhu[1], Weishan Lin[1], Zilong Qiu[2,3], Yizheng Wang[2], Yundong Shen[1,2,4]*, Wendong Xu[1,2,4,5,6,7,8]*

Restoring limb movements after central nervous system injury remains a substantial challenge. Recent studies proved that crossing nerve transfer surgery could rebuild physiological connectivity between the contralesional cortex and the paralyzed arm to compensate for the lost function after brain injury. However, the neural mechanism by which this surgery mediates motor recovery remains still unclear. Here, using a clinical mouse model, we showed that this surgery can restore skilled forelimb function in adult mice with unilateral cortical lesion by inducing cortical remapping and promoting corticospinal tract sprouting. After reestablishing the ipsilateral descending pathway, resecting of the artificially rebuilt peripheral nerve did not affect motor improvements. Furthermore, retaining the sensory afferent, but not the motor efferent, of the transferred nerve was sufficient for inducing brain remapping and facilitating motor restoration. Thus, our results demonstrate that surgically rebuilt sensory input triggers neural plasticity for accelerating motor recovery, which provides an approach for treating central nervous system injuries.

INTRODUCTION

Central nervous system (CNS) injuries, such as stroke, traumatic brain injury (TBI), and spinal cord injury (SCI), are important causes of death and long-term disability worldwide (*1*). These injuries usually disrupt the descending pathway, blocking the transmission of cortical commands from one side of the brain to the opposite side of the spinal cord, resulting in persistent motor functional deficits (*2*, *3*). Many efforts have been devoted to rehabilitation following the acute phase of injury, such as extensive physiotherapy and pharmacologic intervention (*4*, *5*). Although early interventions can improve gross movements, flexible and skilled movements of an affected hand, such as grasping or manipulating objects, remain impaired in most of the patients (*4*). In particular, neurologic recovery usually plateaus at 6 months after injury and is difficult to rehabilitate further (*6*). Therefore, a promising therapeutic approach is to recruit spared circuits in the contralesional (remaining) cortex to rebuild functional connections to the paralyzed (ipsilateral) extremities.

Previously, we reported that crossing nerve transfer surgery, referred to as contralateral seventh cervical nerve transfer (CC7), could be used to treat paralyzed upper extremities in adult patients after chronic unilateral brain injury (*7*). CC7 surgery rewires peripheral nerves by transferring the contralateral seventh cervical (C7) nerve from the nonparalyzed side to the paralyzed side. Patients who underwent this surgery showed significant improvements, especially in skilled movements of the paralyzed hand, as measured using the Fugl-Meyer assessment of motor recovery; this recovery led to improved self-care ability in daily life. In addition, transcranial magnetic stimulation (TMS) and functional magnetic resonance imaging (fMRI) showed the establishment of physiological connectivity between the contralesional cortex and the paralyzed arm. These results indicated that CC7 surgery could stimulate adult neuroplasticity in the contralesional hemisphere, restoring motor control of the ipsilateral paralyzed arm. Intriguingly, as early as 1874, Brown Sequard declared that either side of the human brain was sufficient to innervate both sides of the body (*8*). However, how C7 nerve transfer leads to functional recovery of the paralyzed arm in patients remains unknown. In this study, we first established an experimental model in adult mice that replicates nerve transfer–induced functional recovery. Then, we demonstrate the mechanisms of the establishment of functional circuits that connect the ipsilateral sensory cortex to the paralyzed forelimbs.

RESULTS

Establishment of CC7 surgery in adult mice with unilateral cortical lesions

The brachial plexus (BP) is a network of five nerves from distinct spinal cord segments [C5, C6, C7, C8, and the first thoracic nerve (T1)]. C7 nerve is located in the middle of the BP, and the total number of nerve fibers in the human C7 is approximately 80,000, of which more than 90% are sensory fibers (*9*). Previous studies have revealed that transecting the C7 nerve does not cause permanent functional deficiency, due to the compensation by the C5, C6, C8, and T1 nerves (*10*, *11*). To establish a mouse model of CC7 surgery for the treatment of unilateral TBI, we first used an electric cortical contusion impactor (eCCI) to damage the sensorimotor cortex of the left hemisphere to generate a unilateral cortical lesion (fig. S3, A to C) (*5*, *12*). We performed CC7 surgery 2 weeks later, after the acute injury period (Fig. 1A). The left (healthy side) C7 nerve was dissected and severed as distally as possible, and the right (impaired side) C7

[1]Department of Hand Surgery, Huashan Hospital, Fudan University, Shanghai, China. [2]The National Clinical Research Center for Aging and Medicine, Fudan University, Shanghai, China. [3]Institute of Neuroscience, State Key Laboratory of Neuroscience, Center for Excellence in Brain Science and Intelligence Technology, Chinese Academy of Sciences, Shanghai, China. [4]Department of Hand and Upper Extremity Surgery, Jing'an District Central Hospital, Fudan University, Shanghai, China. [5]Institutes of Brain Science, Fudan University, Shanghai, China. [6]State Key Laboratory of Medical Neurobiology, Collaborative Innovation Center of Brain Science, Fudan University, Shanghai, China. [7]Co-innovation Center of Neuroregeneration, Nantong University, 226000 Nantong, China. [8]Research Unit of Synergistic Reconstruction of Upper and Lower Limbs After Brain Injury, Chinese Academy of Medical Sciences, Beijing, China. *Corresponding author. Email: wendongxu@fudan.edu.cn (W.X.); yundongshen@fudan.edu.cn (Y.S.)
†These authors contributed equally to this work.

nerve was harvested as proximally as possible (*7*). Then, the left C7 nerve root was guided via the prespinal route and microsurgically sutured to the right C7 nerve root (Fig. 1B and movie S1). Because the C7 nerve contains sensory and motor fibers, the descending motor outputs from the left spinal cord can be transmitted to the right forelimb, and the ascending sensory inputs from the right forelimb can be transmitted to the left spinal cord after CC7 surgery (fig. S1A). Electron microscopy revealed that the transferred C7 nerve fibers from the left spinal cord had regenerated across the coaptation site and myelinated (fig. S1B). At 6 weeks post-CC7 surgery, electrically stimulating the C7 nerve proximal to the coaptation site induced stable compound muscle action potential (CMAP) signals in multiple muscles of the affected forelimb (fig. S2). Together, these results suggest that the C7 nerve fibers from the left spinal cord can regenerate through the coaptation site and completely innervate the right forelimb at 6 weeks post-CC7 surgery.

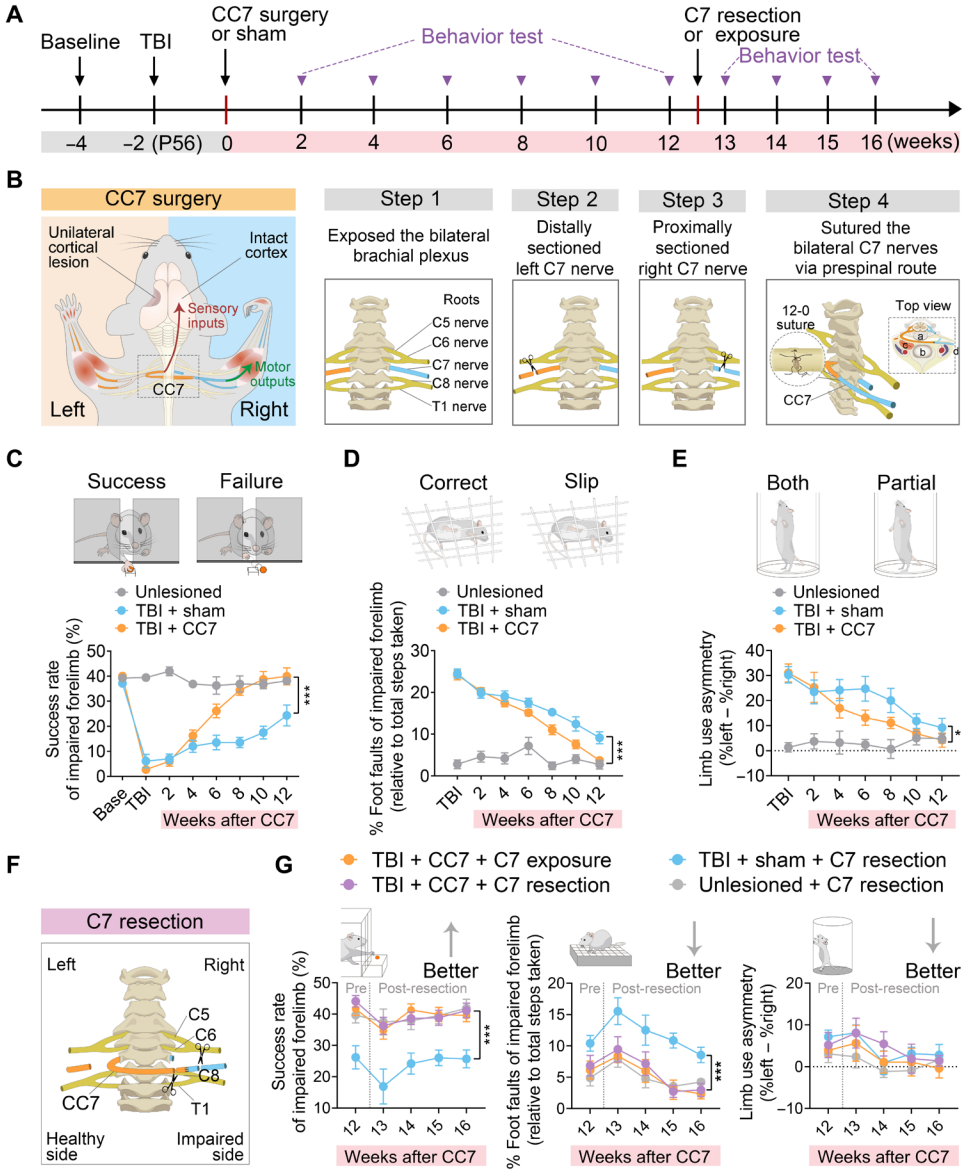

Fig. 1. CC7 surgery restored skilled movements of the impaired forelimb in adult mice following unilateral TBI. (**A**) Timeline of behavioral studies (top) and schematic diagram of the groups of mice (bottom). (**B**) Schematic of the crossing nerve transfer surgery. The diagrammatic drawing of surgical procedures. The C7 nerve originating from the healthy side was surgically transferred to reinnervate the impaired forelimb. (**C** to **E**) Behavioral tests, including single-pellet reaching test (C, $n = 6$ each), grid-walking test (D, $n = 6$ for unlesioned group, $n = 8$ each for other groups), and cylinder test (E, $n = 6$ for unlesioned group, $n = 8$ each for other groups) to evaluate the impaired forelimb function in three groups. CC7 surgery produced a significant recovery in impaired forelimb function compared with TBI + sham group over 2 to 12 weeks after CC7 surgery, respectively, in high success rate (C), low foot faults (D), and balanced limb use symmetry (E). $^{*}P < 0.05$ and $^{***}P < 0.001$, two-way ANOVA. In this and all subsequent figures, statistic results are only comparing the TBI + CC7 group (mice undergoing TBI and CC7 surgery) with TBI + sham group (mice undergoing TBI and sham surgery). (**F**) Schematic of the transferred C7 nerve resection in TBI + CC7 group mice at 12 weeks after surgery. (**G**) Effect of resecting the transferred C7 nerve at 12 weeks after surgery on the behavioral performance of the impaired forelimb in single-pellet reaching test (left), grid-walking test (middle), and cylinder test (right) ($n = 6$ for each group).

In addition, G-deleted rabies virus (RV) modified to express enhanced green fluorescent protein (EGFP) was injected into the transferred C7 nerve distal to the coaptation site to label the regenerated nerve fiber, including motor fibers from the motor neuron in the left ventral horn and sensory fibers from the left C7 dorsal root ganglion (DRG) (fig. S1, C, D, and F). DRG neuron cells, which regenerated axons through the coaptation site and were retrogradely labeled by the rabies virus, were similar to those in nontransfer mice (fig. S1G). The type and distribution of central projections to the spinal cord dorsal horn of DRG neurons with regenerated peripheral projections were consistent with those of DRG neurons in nontransfer mice (fig. S1E). The regenerated motor and sensory fibers reached the right forelimb to form neuromuscular junctions (NMJs) and muscle spindles (fig. S1, H to J). Together, these results suggest that the transferred C7 nerve successfully regenerated, functionally conducting motor and sensory signals via afferent and efferent fibers.

Behavior performance after CC7 surgery and C7 resection

The mice were divided into the unlesioned + sham, TBI + sham, and TBI + CC7 groups. For the sham surgery, we selectively transected the C7 nerve on the left side. Behavioral tests were performed once every 2 weeks over the 12 weeks after surgery in a double-blind manner. In the open-field and the rotarod tests, both considered to reflect gross motor recovery, the TBI + sham group and TBI + CC7 group showed similar continuous spontaneous improvements after the injury, returning to almost normal levels at 6 to 10 weeks after CC7 surgery (fig. S3, F and G, and table S1). However, in contrast to gross motor function, the TBI + sham group showed significant impairments in three behavioral aspects related to skilled motor function, namely, the single-pellet reaching, grid walking, and cylinder tests. The TBI + CC7 group began to show improvements over the TBI + sham group at 6 to 8 weeks after surgery, and almost no difference from the unlesioned group was present at 12 weeks after surgery (Fig. 1, C to E, fig. S3D, and table S1). On the single-pellet reaching test, analysis of reaching trajectories, speed and variability revealed that the reaching task performance of the TBI + CC7 group was more similar to that of the unlesioned group than to that of the TBI + sham group (fig. S3E).

Furthermore, when we resected the transferred C7 nerve at 12 weeks after surgery, the behavioral test showed a minimal reduction in the restored skilled motor function of the impaired forelimb (Fig. 1, F and G, movie S2, and table S1). In addition, the affected forelimb of TBI + sham mice still had significant motor dysfunction even at 16 weeks after CC7 surgery, especially in single-pellet reaching and grid-walking tests. This finding suggests that other neural pathways, in addition to the transferred C7 pathway (contralateral pathway), contribute to the skilled motor functional recovery of the impaired forelimb. The skilled motor function of the impaired forelimb was mostly restored at 12 weeks after surgery, indicating that this newly formed neural circuit was basically complete at that time.

CC7 surgery reconnected the impaired forelimb and the intact cortex

To explore whether and how the number of neurons involved in the control of the skilled motor function of the impaired forelimb would be changed after CC7 surgery, we injected pseudorabies virus (PRV) encoding EGFP into multiple muscles of the impaired forelimb at 12 weeks after surgery (Fig. 2A). At 5.5 days after PRV injection, we specifically identified the distribution of $EGFP^+$ neurons in the TBI + CC7 group mice and determined that most $EGFP^+$ neurons were located in the spinal cord, subcortical areas, and cerebral cortex (fig. S4, A and B). Most of these labeled regions, such as the medulla oblongata and the periaqueductal gray matter, have been identified as motor control–related regions in previous studies (*13*, *14*). In addition, there were more dorsal horn and ventral horn spinal neurons at the healthy side C7 segment labeled with PRV in the TBI + CC7 group compared to the TBI + sham group, indicating that the transferred C7 nerve successfully mediated contralateral innervation of the impaired forelimb (fig. S4, C and D).

Focusing on retrograde tracing in the intact cerebral cortex, we produced horizontal cortical maps of neurons labeled with PRV to further elucidate the distribution pattern of $EGFP^+$ neurons in the contralesional cortex. The cortical maps showed that these neurons were mainly present in the regions caudal to the bregma; specifically, in two separate areas along the rostrocaudal axis, corresponding to the rostral forelimb motor area (RFA) and the caudal forelimb motor area (CFA) (Fig. 2B) (*15*, *16*). The RFA is a premotor area in the secondary motor cortex (M2), whereas the CFA is the initiating region of the cortical sensorimotor system. The CFA can be further divided into two parts, the medial CFA (mCFA), which corresponds to the primary motor cortex (M1), and the lateral CFA (lCFA), which corresponds to the primary sensory cortex (S1) and functions as a sensory forelimb area (SFA) (Fig. 2C) (*15*, *17*, *18*). At 12 weeks after CC7 surgery, we identified an increase in the density of traced neurons in the CFA (Fig. 2, B and D). Furthermore, after the injection of PRV into the left or right forelimb muscles in different animals, an analysis of the different subregions of CFA in right (contralesional) hemisphere revealed that in mice in the TBI + CC7 group, neurons originating from right (healthy) forelimb concentrated in the mCFA, whereas neurons traced from left (impaired) forelimb concentrated in the lCFA (S1) (Fig. 2E and fig. S4, E to I). However, in the unlesioned group and the TBI + sham group, both neurons connecting to the left forelimb and neurons connecting to the right forelimb were concentrated in the mCFA (*14*). Our quantitative analysis of $EGFP^+$ neurons showed that the number of neurons connecting to the left forelimb or right forelimb was both reduced after TBI, which may be due to partial degeneration of motor axon terminals both on the contralateral and ipsilateral side caused by TBI (*19*). The CC7 surgery did not alter the contralateral connection but greatly increased the number of neurons connecting to the ipsilateral forelimb in the lCFA of contralesional cortex (fig. S4, G and H). This distribution pattern after CC7 surgery suggests that the contralesional cortex separated the functional areas of the healthy and impaired forelimbs, and most innervation of the impaired muscles was more innervated by the intact sensory cortex.

At 12 weeks after CC7 surgery, the impaired forelimb is connected to the contralesional cortex through the transferred contralateral C7 nerve and the ipsilateral BP, including the C5, C6, C8, and T1 nerves. We set up two experimental conditions to test whether these two pathways could be traced to different parts of the cortex. We first transected the ipsilateral pathway (C5, C6, C8, and T1) of the impaired forelimb, retaining only the contralateral pathway (contralateral C7) for specific PRV retrograde tracing. In addition, we transected the contralateral pathway (contralateral C7) and retained the ipsilateral pathway (C5, C6, C8, and T1) for PRV retrograde tracing in another TBI + CC7 group. In both cases, traced neurons were mainly located in the S1 cortex (Fig. 2, B and F, and fig. S4, J to L). These results suggest that after motor function recovery, the cortical neurons

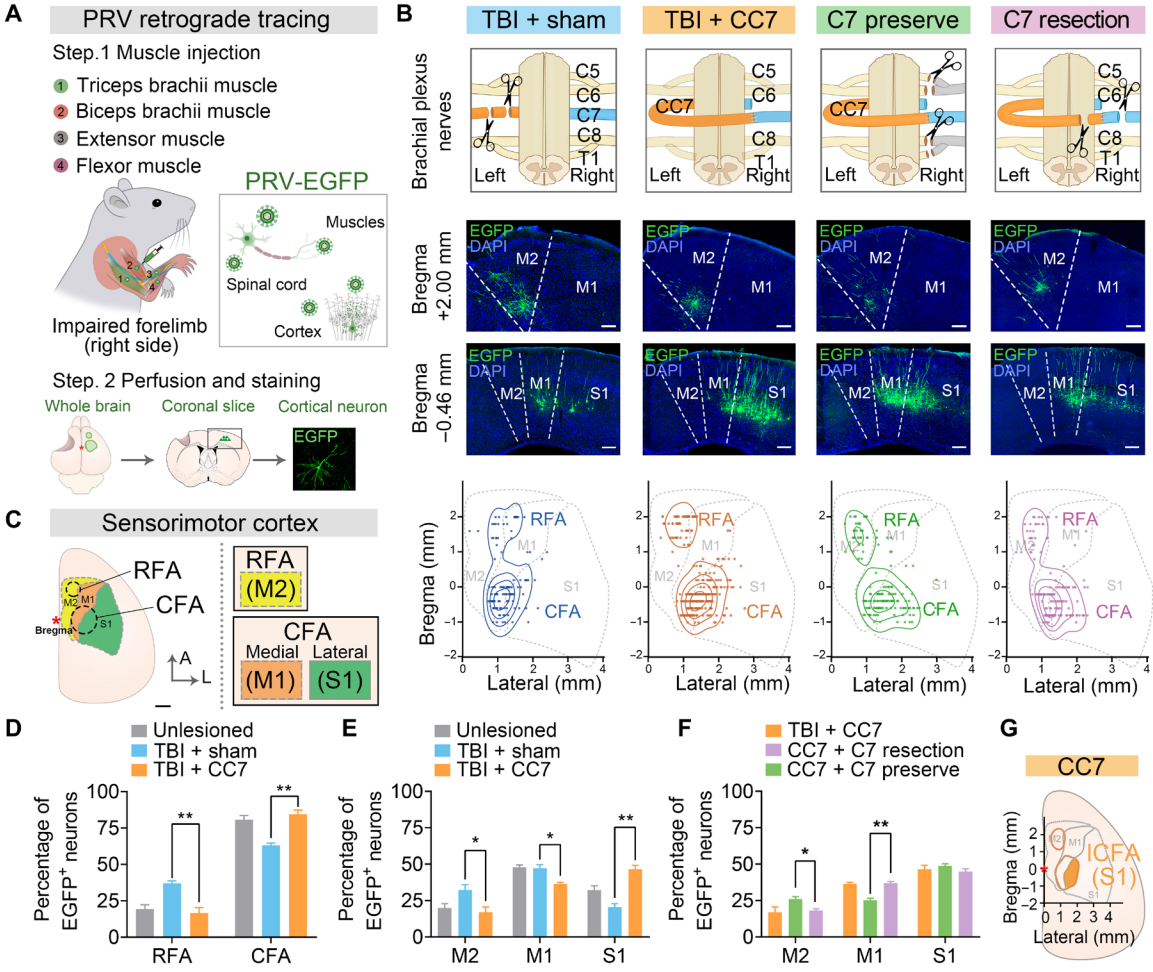

Fig. 2. CC7 surgery reconnected the impaired forelimb and the intact cortex. (**A**) Schematic of PRV-EGFP injection into four forelimb muscles innervated by BP (including biceps, triceps, flexors, and extensors muscle) on the impaired (right) side at 12 weeks after surgery (top) and the strategy of EGFP$^+$ cortical neurons mapping (bottom). (**B**) Schematic of BP nerves in different groups (top). Fluorescence images showing EGFP$^+$ neurons (green) in the different cortical regions of the intact hemisphere traced from the impaired forelimb in all four groups (middle). Scale bars, 200 μm. Plotting of EGFP$^+$ neurons traced from the impaired forelimb (bottom). (**C**) Schematic of dorsal view of the right sensorimotor cortex. Scale bar, 1 mm. Colors indicate conventional functional regions: orange, M1, primary motor cortex; yellow, M2, secondary motor cortex; green, S1, primary sensory cortex, based on Allen Brain Atlas. Forelimb-related motor areas (RFA and CFA) are schematically shown as dotted circles (*15*, *18*, *71*). (**D** and **E**) The percentage of EGFP$^+$ neurons distributed in (C) of the forelimb-related motor areas (D) and the different functional cortical regions (E) in three groups at 12 weeks after surgery ($n = 3$ for unlesioned group, $n = 4$ for other groups). *$P < 0.05$ and **$P < 0.01$, unpaired t test. (**F**) The percentage of EGFP$^+$ neurons distributed in (C) of the different functional cortical regions in three CC7 related groups at 12 weeks after surgery ($n = 4$ for CC7 and $n = 3$ for other groups). *$P < 0.05$ and **$P < 0.01$, unpaired t test. (**G**) Schematic of distribution pattern of EGFP$^+$ neurons in the intact sensorimotor cortex tracing from the impaired forelimb at 12 weeks after surgery. The impaired forelimb-related motor areas are schematically shown as orange hollow circles, and the orange solid circle represents the most significantly increased region in the CC7 group comparing to the TBI group.

in the S1 cortex that were originally connected with the contralateral pathway (contralateral C7) also connect with the impaired forelimb through the ipsilateral pathway (C5, C6, C8, and T1) (Fig. 2G).

CC7 surgery forced the intact SFA to remap to a cortical motor area

To test the functional remapping of the contralesional cortex after CC7 surgery, we determined the SFA in response to sensory stimulation by performing wide-field calcium imaging in *Thy1-GCamp6s* mice (Fig. 3A). In general, sensory stimulation of the forepaw results in localized cortical responses in the sensorimotor cortex contralateral to the stimulated side (*20*). As expected, among the unlesioned group, TBI + sham group, and TBI + CC7 group, we found that sensory stimulation of the left (healthy) forepaw could produce calcium signals in the contralesional cortex (Fig. 3B and fig. S5, A, C, and D). The SFA of the left forelimb in the contralesional hemisphere included both the M1 and S1 cortices, and the intensity of the calcium signal in the S1 cortex was higher than that in the M1 cortex among the three groups (fig. S5D). However, when we stimulated the right (impaired) forepaw, only the TBI + CC7 group had a calcium response in the contralesional cortex (Fig. 3B and fig. S5, A and B). Similar to that in the left forelimb, the SFA of the right forelimb consisted of the M1 cortex and S1 cortex (Fig. 3C and fig. S5B). However, there was no significant difference in calcium signal intensity between the M1 cortex and S1 cortex, indicating that the SFA of the right forelimb was located more medially than that of the left forelimb (fig. S5D).

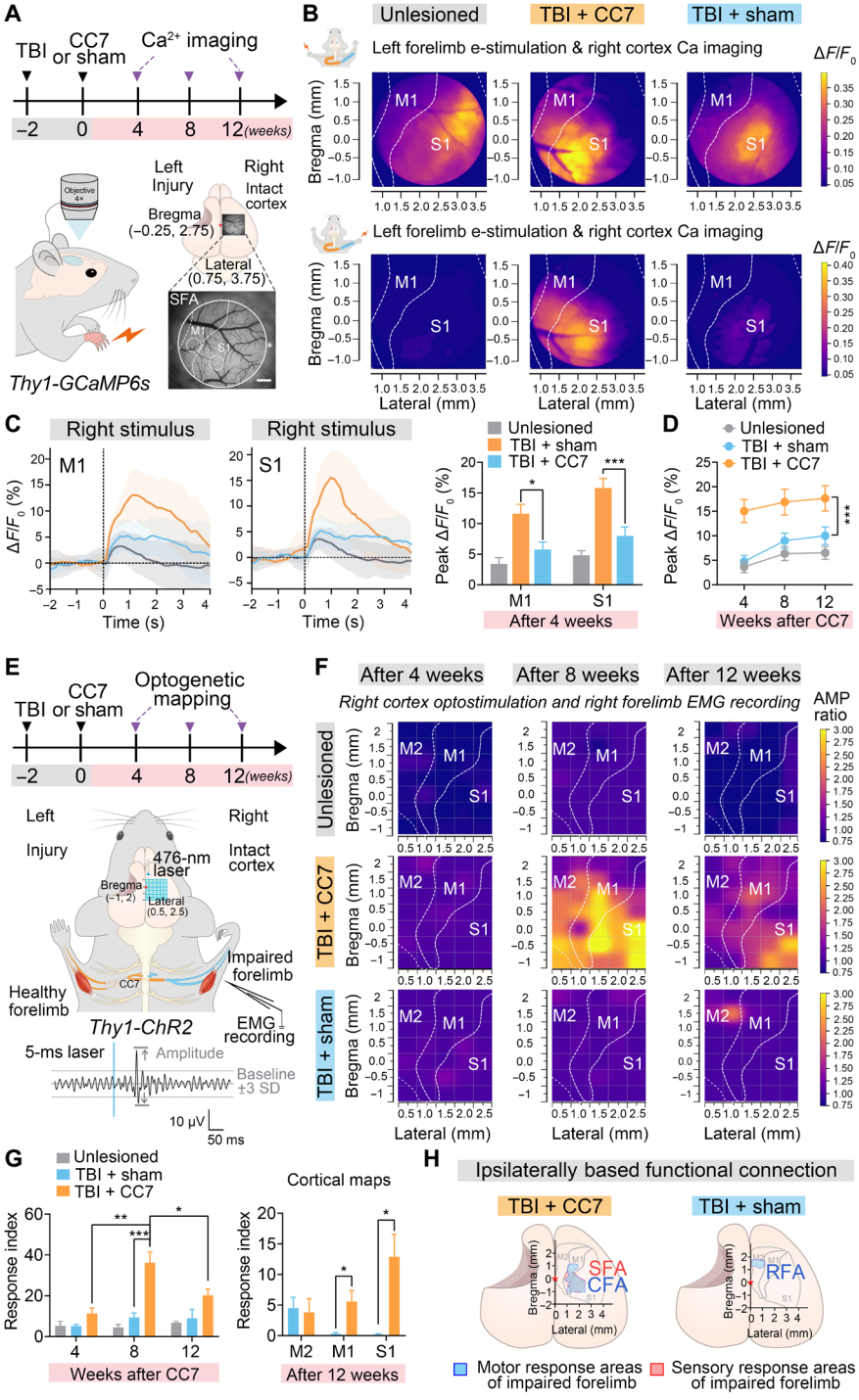

Fig. 3. CC7 surgery forced the intact SFA to remap to a new motor representation area. (**A**) Timeline of the wide-field Ca^{2+} imaging. White circle indicates the region of interest (ROI). White dotted circles indicate the analyzed regions of M1 and S1. Scale bar, 500 μm. (**B**) Example fluorescent responses elicited by electrical stimulation of left (top) or right (bottom) forepaws in the unlesioned (left), TBI + CC7 (middle), or TBI + sham (right) mouse at 4 weeks after surgery. (**C**) Quantitative comparisons of the M1 (left) and S1 (middle) cortex fluorescent responses in (B) ($n = 6$ for unlesioned and $n = 7$ for other groups). Right: $\Delta F/F_0$% (peak amplitude fluorescent response) of M1 and S1 cortex in three groups. *$P < 0.05$ and ***$P < 0.001$, unpaired t test. (**D**) $\Delta F/F_0$% of the ROI region after right stimulus in the three groups at different times after surgery. ***$P < 0.001$, two-way ANOVA. (**E**) Timeline and schematic of optogenetics-based motor mapping. Optostimulations were delivered using a mapping grid positioned over the sensorimotor cortex, as shown in the illustration. The amplitude of motor evoked potentials recorded in the tricep brachii of the affected forelimb was measured for each site of stimulation to elaborate a motor map. (**F**) The average heatmaps of unlesioned (top), TBI + CC7 (middle), and TBI + sham (bottom) mice at different times after surgery ($n = 3$ for unlesioned, $n = 8$ for CC7, and $n = 6$ for TBI groups). (**G**) Quantitative analysis of the response index in three groups at different times after surgery (left) and in different cortical regions of TBI and CC7 groups at 12 weeks after surgery (right). *$P < 0.05$, **$P < 0.01$, and ***$P < 0.001$, unpaired t test. (**H**) Motor and sensory cortical forelimb representations of TBI + CC7 and TBI + sham groups.

This phenomenon in the TBI + CC7 group appeared 4 weeks after surgery and then became stable at 8 and 12 weeks after surgery (Fig. 3D). Thus, these results revealed that CC7 surgery can transmit sensory inputs from the affected forelimbs to the SFA in the contralesional medial sensorimotor cortex.

Next, we evaluated the cortical motor representation of the bilateral forelimb by optogenetically manipulating the activity of the cortex on the contralesional side and recording electromyograms (EMGs) of forelimb muscle from *Thy1-ChR2* mice at multiple time points after surgery (Fig. 3E). The motor response areas of the left forelimb were similar in the three groups (fig. S5E). Consistent with previous studies, the motor representation of the right forelimb in the TBI + sham group with spontaneous recovery was mapped to the RFA (Fig. 3, F and H) (*16*, *21*). However, in the TBI + CC7 group, the contralateral cortex showed a wide range of response areas, including the RFA and CFA, at 8 weeks after surgery. This range was reduced and concentrated to the lCFA at 12 weeks after surgery (Fig. 3, F and H). This finding is consistent with fMRI trends in clinical patients (*7*). We designed a response index defined as the ipsilateral response amplitude multiplied by the response area to quantify the extent of cortical motor representation. Quantitative analyses suggested that the response index of the right forelimb was significantly increased in the TBI + CC7 group compared to the TBI + sham group over 8 to 12 weeks after surgery and was mostly located in the CFA, including the M1 and S1 cortices (Fig. 3G). By drawing the ranges of cortical response areas, we found that the cortical motor areas of the right forelimb greatly overlapped with the SFA in the TBI + CC7 group (Fig. 3H).

Therefore, these results revealed that at 12 weeks after surgery, the SFA of the right forelimb was remapped to the medial part of sensorimotor cortex, while the motor response area was remapped to the lateral part of sensorimotor cortex (fig. S5F). These data suggested that the SFA was gradually remapped to a cortical motor area of the impaired forelimb and stabilized following motor recovery, thus allowing functional recovery from brain injury.

CC7 surgery promotes ipsiCST regrowth to dominate the motor recovery process

Previous studies have proven that the formation of descending circuits related to motor recovery relies on the ability of cortical neurons to establish new connections after brain injury (*22*). To investigate the projection patterns of cortical neurons of the motor response area in different groups, two types of adeno-associated viruses (AAV), AAV-CaMKII-ChR2-EYFP and AAV-CaMKII-ChR2-mCherry, were injected separately into the SFA and RFA of mice in the TBI + CC7 and TBI + sham groups (Fig. 4A and fig. S6, A and B). The density and number of midline-crossing fibers (ipsilateral projection CST fibers, ipsiCST fibers) from the SFA-originated EYFP-labeled CST to the spinal cord on the ipsilateral impaired side were significantly increased in the TBI + CC7 group, especially in the segments innervating the BP, including the C5, C6, C7, C8, and T1 nerves (Fig. 4, B and D). The number of sprouting axons became significantly higher at 4 weeks, peaked at 8 weeks and then declined at 12 weeks after surgery (Fig. 4C). We also found that the ipsiCST fibers in the TBI + CC7 group exhibited a wide distribution in the subcortical areas and lumbar spinal cord (fig. S6, F and J). Optostimulation of the EYFP-labeled neurons in contralesional SFA stably activated the biceps brachii, triceps brachii, extensor, and flexor muscles of impaired forelimbs in the TBI + CC7 group at 8 weeks after CC7 surgery (fig. S6K). Comparing to the TBI + sham groups, the normalized response of the EMG signal in the impaired forelimb was higher in the TBI + CC7 group, especially in the flexor muscle innervated by the lower trunk (fig. S6L). In addition, such ipsiCST fibers appeared to have a widespread distribution across different laminae in cervical spinal cord, including the dorsal and ventral horns (Fig. 4E). In the TBI + CC7 group, EYFP-labeled axons from the SFA exhibited profound sprouting in the dorsal and ventral regions, predominantly both in sensory laminae 3 to 5 and motor laminae 6 to 8 (Fig. 4E and fig. S6, D and E). In contrast, mCherry-labeled RFA CST axon sprouting in the TBI + sham group was more pronounced in the motor laminae 6 to 8 (fig. S6, C to E). These results suggest that crossing nerve transfer promotes axonal sprouting from intact SFA cortical neurons to the denervated side of the spinal cord, which reinforces innervation of the impaired forelimb.

To determine the distribution pattern of corticospinal neurons (CSNs) after CC7 surgery, viruses encoding retro AAV-EGFP and retro-AAV-tdTomato were injected separately into the healthy and impaired sides of the seventh cervical spinal cord (fig. S7A). As shown in fig. S7B, the number of tdTomato-labeled ipsilateral projection CSNs (ipsiCSNs) was significantly increased after CC7 surgery. Notably, most of the tdTomato-labeled ipsiCSNs were colabeled with EGFP, suggesting that these neurons were originally connected to the healthy-side spinal cord and then reconnected with the impaired forelimb through collateral sprouting (fig. S7, C and D). After skilled motor function of the impaired forelimb was restored, pharmacogenetic suppression of the neuronal activities of such ipsiCSNs abolished the improvement in behavioral performance (Fig. 4, F to H; fig. S7, E to I; and table S1), as observed in previous studies. Thus, ipsiCSNs play a vital role in maintaining recovered skilled movements.

Ipsilateral sensory inputs mediated by the transferred C7 nerve are essential for motor recovery

To further explore the function of the transferred C7 nerve (contralateral projection CST, conCST), at 2 weeks after CC7 surgery, when the nerve fibers of the transferred C7 nerve had not completely innervated the affected forelimb at this time (fig. S8A), we resected this nerve distal to the coaptation site and performed behavioral tests 4, 8, and 12 weeks later (Fig. 5A and movie S2). The behavioral tests showed that the skilled motor function of the affected forelimb was no longer restored in these mice (Fig. 5B). We then performed anterograde tracing from the intact SFA in these mice, and the results revealed rare axonal sprouting across the midline to the spinal cord on the impaired side (Fig. 5C and fig. S8, C and D). Then, we resected the transferred C7 nerve at 8 weeks after CC7 surgery (Fig. 5A). Unlike C7 resection at 2 weeks after surgery, the skilled motor function of the affected forelimb in 8 weeks C7 resection group continuously improved up to 12 weeks after CC7 surgery (Fig. 5B and table S1). The anterograde tracing analysis of the intact SFA confirmed the formation of an intrinsic ipsiCST (Fig. 5C and fig. S8, C and D). Moreover, we conducted optogenetic stimulation mapping and found that the EMG signals were still generated in the impaired forelimb when stimulation was concentrated at the intact SFA (fig. S8B). Similar to that observed with the PRV retrograde tracer analysis, this finding confirmed that intact SFAs innervated the right forelimb through ipsilateral pathways (C5, C6, C8, and T1). Thus, the transferred C7 nerve (conCST) plays a vital role in the early period after surgery and triggers the ipsiCST, whereas behavioral improvement in the impaired forelimb is less dependent on the C7 nerve.

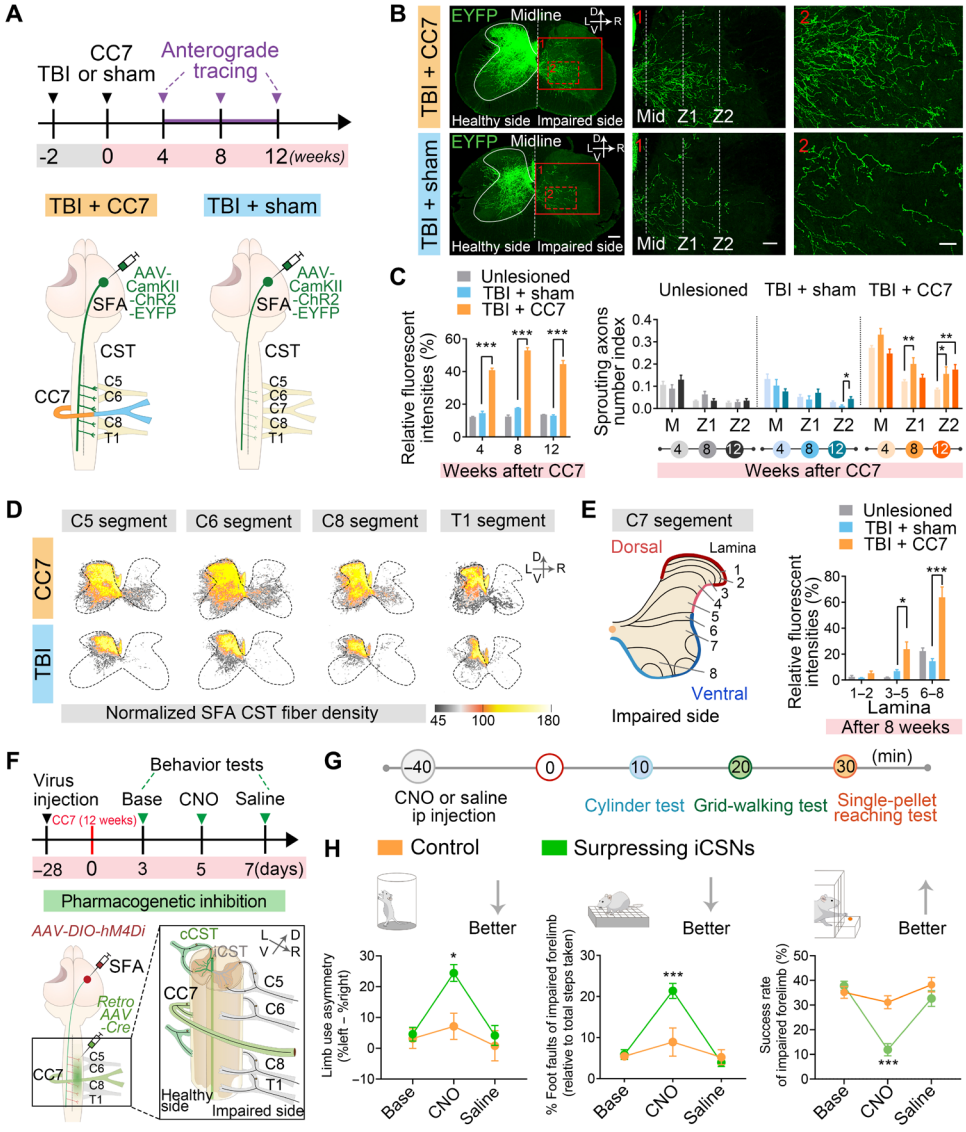

Fig. 4. The ipsiCST regrowth from the intact SFA to the affected spinal cord. (**A**) Top: Timeline of AAV virus–based anterograde tracing. Bottom: Scheme illustrating the strategy for labeling the CST axons from SFA in TBI + CC7 and TBI + sham group. (**B**) Transverse C7 cervical cord sections showing SFA CST axons sprouting in TBI + CC7 animals (top) and TBI + sham animal (bottom) at 8 weeks after surgery. Scale bar, 200 μm. (1) The white dashed lines for intersection counts with corticospinal fibers. Scale bar, 100 μm. (2) Axon branches of uninjured CST fibers on the paralyzed side. Scale bar, 50 μm. (**C**) Quantifications of relative fluorescence intensity (left) and sprouting axon number index (right) in the three groups at 4, 8, and 12 weeks after surgery ($n = 3$ each). *$P < 0.05$, **$P < 0.01$, and ***$P < 0.001$, two-way ANOVA. (**D**) Heatmaps are shown for a representative image from the TBI + CC7 group (top) and TBI + sham group (bottom) along the gray matter in other segments at 8 weeks after surgery. (**E**) Schematic diagram of the different laminae of the C7 spinal cord (left). Quantifications of relative fluorescence intensity in three groups at different spinal cord lamina at 8 weeks after surgery (right, $n = 3$ each). *$P < 0.05$ and ***$P < 0.001$, two-way ANOVA. (**F**) Experimental timeline of pharmacogenetic suppression (top). Schematic diagram of virus injections into the contralesional SFA cortex (AAV-hSyn-Dio-hM4Di-mCherry) and denervated cervical spinal cord (retro-AAV-hSyn-Cre or retro-AAV-hSyn-EGFP as control) at 12 weeks after surgery (bottom). L, left side; V, ventral side; D, dorsal side; R, right side. (**G**) Timeline of behavioral studies. (**H**) Effect of suppressing the neuronal activity of corticospinal neurons in intact SFA on cylinder test (right), grid-walking test (middle), and single-pellet reaching test (left) at 12 weeks after surgery ($n = 8$ each). *$P < 0.05$ and ***$P < 0.001$, two-way ANOVA. ip, intraperitoneal.

The transferred C7 nerve consists of a mixture of both motor and sensory fibers. We next determined the effect of sensory and motor components in the transferred peripheral nerve on the rewiring of the intact CST circuit. At 2 weeks after CC7, the ventral root containing motor fibers of the transferred C7 was surgically cut in one group of mice, retaining only sensory fibers in the transferred C7 nerve (TBI + CC7 + sensory fibers preserved group) (movie S3). In contrast, in the other group, the dorsal root containing sensory fibers of the transferred C7 was cut, leaving the transferred C7 with only motor fibers (TBI + CC7 + motor fibers preserved group) (Fig. 5D and movie S4). Both groups were then observed for 12 weeks. We next injected RV-EGFP at the distal end of the C7 nerve coaptation site and found that EGFP-labeled fibers and cell bodies could be observed in the spinal dorsal horn and DRG of mice in the TBI + CC7 + sensory fibers preserved group at 1 month after CC7 surgery (fig. S9, A to C). Similarly, EGFP-labeled cell bodies were observed

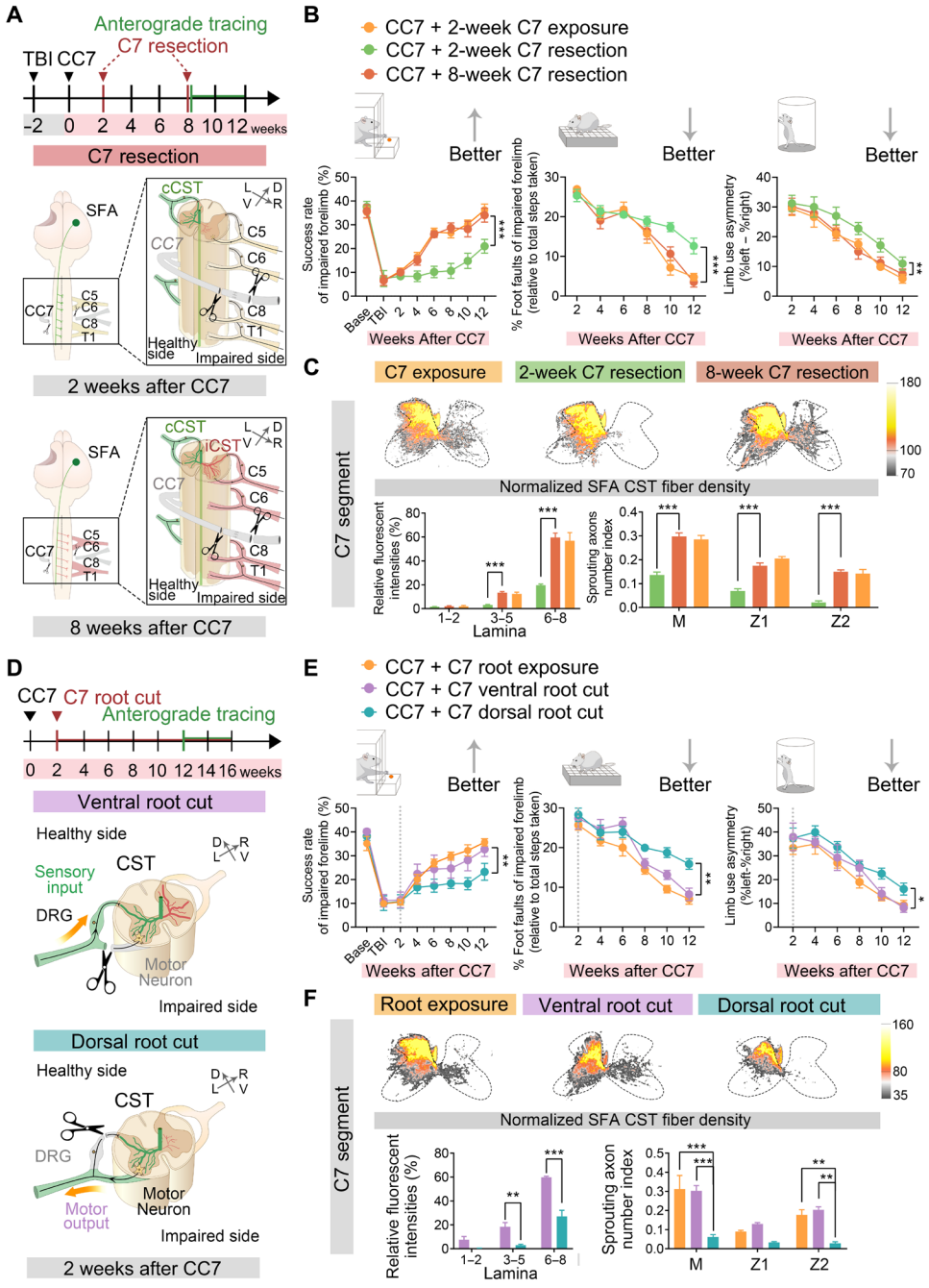

Fig. 5. The transferred C7 nerve–mediated sensorimotor pathway is necessary for triggering ipsiCST formation but not for motor improvement. (**A**) Timeline of C7 nerve resection at 2 or 8 weeks after surgery. Scheme illustrating C7 nerve resection at 2 weeks (middle) or 8 weeks (bottom) after surgery. (**B**) Single-pellet reaching test (left), grid-walking test (middle), and cylinder test (right) scores in three groups ($n = 6$ each). $^{**}P < 0.01$ and $^{***}P < 0.001$, two-way ANOVA. (**C**) Top: Heatmaps were shown for a representative image from the intact SFA CST axons sprouting in TBI + CC7 + 2-week exposure animal (left), TBI + CC7 + 2-week resection animal (middle), and TBI + CC7 + 8-week resection animal (right) along the gray matter in the C7 segment at 12 weeks after surgery. Bottom: Quantification of the relative fluorescence intensity at different spinal cord laminae (left) and sprouting axon number index (right) in the three groups at 12 weeks after surgery ($n = 3$ each). $^{***}P < 0.001$, two-way ANOVA. (**D**) Timeline of C7 nerve rootlets cut (top). Scheme illustrating CC7 + C7 ventral or dorsal root cut at 2 weeks after surgery (bottom). (**E**) Single-pellet reaching test (left), grid-walking test (middle), and cylinder test (right) in three groups ($n = 6$ for CC7 + C7 root exposure, $n = 10$ for CC7 + C7 ventral root cut and dorsal root cut groups). $^{*}P < 0.05$ and $^{**}P < 0.01$, two-way ANOVA (only comparing the CC7 + C7 ventral root cut and dorsal root cut groups). (**F**) Top: Heatmaps are shown for a representative image from three groups along the gray matter in the C7 segment. Bottom: Quantifications of relative fluorescence intensity (left) and the sprouting axon number index (right) in (top). $n = 3$ for each, $^{**}P < 0.01$ and $^{***}P < 0.001$, two-way ANOVA.

in the spinal ventral horn of mice in the TBI + CC7 + motor fibers preserved group (fig. S9A). These results imply that resection of the anterior or posterior roots of the transferred C7 nerve can effectively block motor or sensory transmission.

We also performed wide-field calcium imaging to functionally identify whether the sensory inputs could be transmitted from the impaired forepaw to the intact sensory cortex in these mice. At 4 weeks after CC7 surgery, in the TBI + CC7 + motor fibers preserved group, the sensory response induced by impaired forepaw stimulation was eliminated. However, in the TBI + CC7 + sensory fibers preserved group, the sensory response remained (fig. S9, D to F). Behavioral tests showed that skilled motor recovery of the impaired forelimb in the TBI + CC7 + motor fibers preserved group was significantly lower than that in other groups (Fig. 5E and table S1). Furthermore, anterograde tracing from the intact SFA also demonstrated robust axonal sprouting across the midline to the spinal cord on the impaired side in the TBI + CC7 + sensory fibers preserved group (Fig. 5F and fig. S9G). These findings further verified our aforementioned findings (see the "CC7 surgery forced the intact SFA to remap to a cortical motor area" section), indicating that the transferred C7 (contralateral pathway) transmits the ipsilateral sensory input from the impaired to the SFA, inducing plasticity and forming the ipsilateral pathway that ultimately maintains the improvement in skilled motor function.

Ipsilateral sensory inputs induce a distinct transcriptional profile involved in axonal regeneration

We next investigated the molecular mechanisms underlying crossing nerve transfer by using RNA sequencing (RNA-seq) of SFA tissue (Fig. 6A and table S2). Unsupervised gene expression clustering showed marked changes in gene expression in the intact sensory cortex in the CC7 group (Fig. 6B and fig. S10, A to C). Functional classification of the genes showing surgery-induced expression changes in the sensory cortex demonstrated that surgery strongly stimulated brain plasticity (Fig. 6C). Quantitative analysis of surgery-induced gene expression revealed the enrichment of genes involved in axonogenesis, axon development, and synapse organization (Fig. 6D and fig. S10, D to F). These results illustrated that crossing nerve transfer exerts a beneficial effect by inducing adult neuroplasticity, especially the emergence and elongation of axonal projections, a set of processes that are implicated in brain development and repair (*23*, *24*).

To identify specific molecular targets of pyramidal neurons from the SFA cortex, we performed single-nucleus RNA-seq (snRNA-seq) on SFA cells from CC7 and TBI mice (table S3). We identified over 20 cell clusters by cell type–specific markers, including interneurons, intratelencephalic neurons, pyramidal neurons, and other types of cells (Fig. 6, E and F, and fig. S11, A to C). Gene Ontology (GO) analysis of differentially expressed genes (DEGs) in interneurons between CC7 mice and cTBI mice identified that CC7 surgery up-regulated functions related to cell junctions, growth factor binding, endothelial cell development, and angiogenesis in interneurons while down-regulating the activity of various ion channels (fig. S11, D and E). These results indicated that the interneurons in the SFA area after CC7 had undergone plastic changes similar to those during brain development. While weakening the original electrical activity, interneurons interact with vascular endothelial cells to promote angiogenesis and neuronal migration and accelerate remodeling of connections between cells (*25*, *26*). Because interneurons can directly interact with projection neurons (*27*), we performed a functional analysis of the DEGs between intratelencephalic neurons and pyramidal neurons. Most of the intratelencephalic neurons in the SFA specifically express the layer 2/3 marker genes cux2 and calb1 (*28*), but their projection ability and synapse formation ability did not change significantly after CC7 surgery (fig. S11, F and G). However, pyramidal neurons that specifically express layer 5/6 marker genes such as orpk1 and etv1 showed positive regulation of functions associated with postsynaptic membrane organization, axonogenesis, and axon guidance, suggesting increased pyramidal neuron projecting potential in CC7 mice (Fig. 6G). Meanwhile, the expression of genes related to neuron death, negative regulation of development and growth, and negative regulation of axonogenesis among these pyramidal neurons were reduced in the CC7 group (Fig. 6H). Corticospinal neurons are pyramidal neurons located in layer 5/6 of the cortex. Therefore, these results provide another layer of evidence that plasticity changes in the SFA area caused by crossing nerve transfer are achieved by changing the functions of interneurons and pyramidal neurons (fig. S11H).

DISCUSSION

Recently, many studies have recognized the important role of sensory input in motor function recovery. Sensory signals can affect motor functions by inputting external environmental information and intrinsic physiological status and by guiding the initiation of the motor system (*29*, *30*). Given its demonstrated role in motor control, modifications of sensory input or sensory-motor interactions have potential as a therapeutic strategy after brain damage. However, no effective intervention can directly transmit sensory information from the impaired limb to the contralesional cortex. Our previous studies have shown that CC7 surgery, as a bidirectional transmission pathway between the contralesional hemisphere and the paralyzed hands, can effectively restore skilled forelimb function in adult patients after brain injury (*7*). Our results suggested that surgically rebuilt ipsilateral sensory input is the mechanism by which CC7 surgery improves skilled movements of the impaired forelimb in adult mice with unilateral cortical lesions.

In this study, we used the TBI mouse model to explore the underlying mechanism of skilled motor function restoration of paralyzed forelimb after CC7 surgery. Although there was obvious spontaneous recovery of the affected forelimb function in mice after TBI, some skilled motor functions closely related to CST could not be recovered (*31*, *32*). We demonstrated that CC7 surgery improve the skilled motor function by promoting the axon sprouting of CST in the contralesional sensorimotor cortex. Comparing with other models, such as pyramidotomy lesion, we believe that TBI can better simulate the pathological state after unilateral cortical lesion and contribute to research the remolding of contralesional hemisphere better (*33*). However, clinical studies have confirmed that CC7 surgery has good effects on patients with hemiplegia caused by various diseases (*7*, *34*), the CST changes in various disease models of different species need to be evaluated in future study.

Animal studies have revealed that neonatally pyramidotomied rats can separately control impaired and healthy forelimbs, mainly due to the development of a new motor representative area of the impaired forelimb in the RFA region of the intact cortex (*21*). CSNs in the RFA terminate at all C2 to C7 levels and connect to premotor neurons, mostly innervating the proximal muscles. Similar to the results observed with spontaneous recovery from CNS injuries sustained at a young age, the intact cortex dominated bilateral forelimb

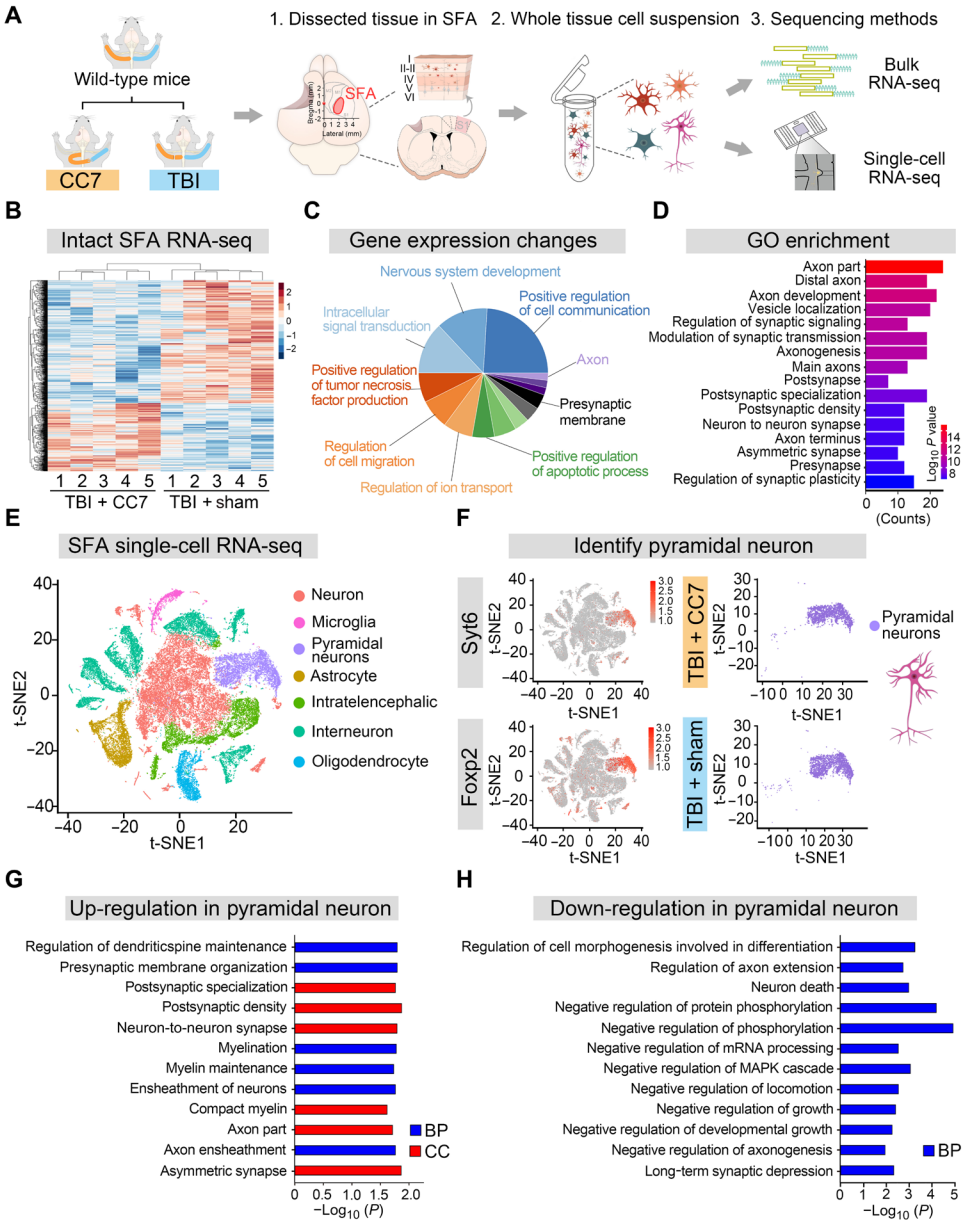

Fig. 6. Establishing ipsilateral sensory inputs change the transcriptome in intact SFAs during the period of CC7 treatment. (**A**) Schematic of the experimental design. SFA sections were isolated for bulk RNA-seq and snRNA-seq experiments. (**B**) Heatmap of the DEGs in TBI + CC7 mice and TBI + sham mice at 4 to 6 weeks after surgery ($n = 5$ each). $P < 0.05$. The color scale represents arbitrary expression units (lowest, blue; highest, red). (**C** and **D**) Gene set enrichment analysis of up-regulated genes in TBI + CC7 mice compared to TBI + sham mice. $P < 0.05$. (**E**) *t*-distributed stochastic neighbor embedding (t-SNE) plots showing the diversity of single-cell events captured in snRNA-seq datasets. Events from TBI + CC7 mice and TBI mice were combined ($n = 3$ each). (**F**) Feature plot of canonical markers defining pyramidal neurons cell types. (**G** and **H**) GO analysis of up-regulated genes (G) and down-regulated genes (H) in the pyramidal neuron cluster in TBI + CC7 mice compared to TBI + sham mice. MAPK, mitogen-activated protein kinase.

control in adult animals with TBI (*16*). Here, we determined that CC7 surgery forces the intact SFA area to remap to a new cortical motor area. There are far more sensory axons than motor axons in the C7 nerve (*9*). After C7 nerve transfer, although the regenerated sensory axons cannot directly affect the motor neurons in the ventral horn (*35*), they can effectively transmit the sensory information from the impaired forelimb to the intact hemisphere (*36*), especially in the SFA rather than the RFA. Calcium imaging results showed that regenerated sensory axons could transmit a variety of sensory information, including mechanosensory and proprioception, to the CNS. Different sensory information is transmitted to the cortex through different ascending pathways, and clarifying the role of different sensory information in CC7 surgery induced cortical reorganization can provide a reference for clinical rehabilitation.

The sensory representation area of the impaired forelimb also received sensory input from the healthy forelimb, which disrupted the original excitatory/inhibitory balance in the SFA. The regional CSNs exhibited robust axonal sprouting from the intact SFA to the

denervated side of the spinal cord in response to the enhancement of neuronal activity. There are two potential underlying circuit mechanisms: (i) CSN activity of layer 5 is significantly increased with the enhancement of layer 2/3 neuron activity through the layer 2/3 to layer 5 local projection in the cerebral cortex (*37*, *38*), and (ii) the thalamus can also activate the CSNs of layer 5 directly via the thalamocortical projection (*39*, *40*). Therefore, we assumed that once the intact SFA receives sensory signals from the impaired forepaw, similar to the domino effect, it alters the level of activity in cortical neurons and reorganizes the cortical map structure to optimize the recovery of skilled motor function.

Previous studies have concluded that the ipsilateral motor pathway from the unaffected sensorimotor cortex to the affected extremity is one of the mechanisms of motor recovery following brain injury (*32*, *41*). Current strategies to modulate such cortical circuit formation in humans include mostly rehabilitative training and, in experimental models, optogenetic stimulation or genetic intervention. However, all of these treatment options have achieved only limited success thus far. In addition to these findings, our team was the first to reveal that crossing nerve transfer could also induce the establishment of ipsilateral motor pathways. Our results showed that the reconstructed ipsilateral motor pathway originating from the contralesional SFA was connected to not only the C7 segment of the spinal cord but also to the whole cervical spinal cord (C5, C6, C8, and T1). Earlier research indicated that the descending output from the somatosensory cortex to the dorsal horn via the CST mediates powerful sensory processing facilitation in the spinal cord, amplifying ascending signal transmission to the brain (*42*). Our results verified that the sprouting axons of ipsiCSNs extend into the dorsal horn, which may constantly amplify the sensory inputs of the affected forelimb, and the ventral horn to control forelimb movements. Previous studies have found that the CST originating from the S1 predominately projects to the dorsal horn and connects to vesicular glutamate transporter type 3 positive ($VGLUT3^+$) interneurons (*14*). Meanwhile, S1 CST also projects to the intermediate gray matter of the cervical spinal cord (laminae 5 to 8) and affects the locomotion of hindlimbs through the relay neurons in the cervical spinal cord (*43*). However, after CC7 surgery, the regrowth ipsiCST located in the medial S1 area (SFA) could project more to the ventral horn, suggesting that CC7 surgery induced reorganization of the spinal cord circuits.

In addition to the ipsiCST, however, several other descending motor pathways stemming from subcortical structures, including the reticular formation and red nucleus, can also contribute to limb movements (*44*). While these subcortical structures contribute to muscle movements, they also interact with cortical motor regions. Furthermore, the severity of lesion is closely related to the compensatory mechanisms after unilateral brain injury (*4*, *45*). The perilesional area compensated for the functional loss in the event of mild or moderate cortical lesion, while the compensation after severe injury relied on the contralesional cortex. Here, we found that after unilateral severe brain injury, CC7 surgery can improve the compensatory ability of the contralesional hemisphere and restore the motor function of the affected forelimb. However, it is unclear whether the mechanism of CC7 surgery is different with various degrees or locations of unilateral brain injury. The role of the ipsilaterally descending pathways and the lesioned hemisphere in motor restoration with CC7 surgery after brain injury needs to be classified in future studies. In addition, whether CC7 surgery in unlesioned mice can lead changes of functional brain network needs to be further elucidated.

The study results indicate that ipsilateral sensory inputs, functioning as triggers, are sufficient to stimulate neural plasticity to restore skilled motor control in adults after brain injury. Current methods, such as proprioceptive neuromuscular facilitation and brain-computer interfaces (BCIs), can precisely modulate sensory inputs from the impaired forelimb (*46*–*48*). In the future, BCIs combined with other approaches, such as neuromuscular electrical stimulation (NMES)-based cycling, may be used to transmit sensory information from the affected limb to the contralesional brain to stimulate plasticity in the adult brain without surgery and to achieve rehabilitation after brain damage (*46*, *49*). Similar concepts may be applied for SCI in which brain plasticity is critical for restoring functional capacity after injury (*38*, *48*, *50*). Therefore, reconstructing sensory inputs is a powerful intervention to recall dormant plasticity in the adult brain, providing a new therapeutic approach to clinical treatment.

MATERIALS AND METHODS

Animals

Male *C57BL/6N*, *Thy1-ChR2*, *Thy1-GCamp6s* mice were used for experiments. *C57BL/6N* mice were purchased from SLAC Laboratory (Shanghai). *Thy1-ChR2* (JAX007612), *Thy1-GCamp6s* (JAX031892), and *Thy1-YFP* mice (JAX 003709) were initially acquired from The Jackson Laboratory. All mice were raised on a 12-hour light/dark cycle (lights on at 7:00 a.m.) with ad libitum food and water. Animals were allocated randomly into different groups where appropriate. All behavioral tests were carried out during the light phase. All procedures were approved by the Animal Care and Use Committee of Huashan Hospital of Fudan University.

Traumatic brain injury

TBI was commonly applied by a well-established procedure as described previously (*12*, *51*). The adult mice aged 8 weeks and weighed between 22 and 25 g were selected as subjects. Briefly, under the pentobarbital sodium (100 mg/kg; Mytechnologies Technologies) anesthesia, mice were placed in a stereotaxic apparatus (RWD Technology Corp. Ltd., Shenzhen, China) with the skull exposed by midline scalp incision. Then, mice received a 4.0-mm-diameter craniectomy, a removal of part of the skull, using an electric microdrill. The coordinates of the craniectomy were anteroposterior (AP) = −1.0 to +2.0 mm and mediolateral (ML) = 0.5 to 3.5 mm. Any animal that experienced excessive bleeding due to disruption of the dura was removed from this study. After the craniectomy, the contusion was induced by eCCI (Virginia Commonwealth University, VCU) with an outfitted with a pounding head 3.0 mm in diameter (*52*, *53*). The impact contusion depth was set to 1.25 mm from dura with a preset velocity of 4.0 m/s sustained for 100 ms. These injury parameters were chosen to target the forelimb motor cortex of the left hemisphere. Animals in the unlesioned group received craniectomy surgeries but without injury. The absorbable hemostatic sponges were used to stanch bleeding, saturate the skin, and maintain temperature throughout the operation.

Contralateral CC7 surgery procedure

The crossing nerve transfer surgery was performed as previously described (*54*, *55*). Briefly, a supraclavicular incision was made to expose the sternum after anesthetizing and placing a mouse in a supine position. A 3-mm median sternotomy incision was made to present the bilateral common carotid artery. At the lateral edge of the left internal jugular vein, the fascia and adipose tissue were pulled outward

to expose the BP. The superior trunk, composed of the C5 and C6 nerves, has three branches. The middle trunk composed of the C7 nerve and inferior trunk composed of C8 and T1 nerves can be identified along the upper trunk to the tail of the mouse. On the left side (donor side), the anterior division and posterior division of the middle trunk (C7 nerve) were dissected distally to the division-to-cord level under the clavicle, and the C7 nerve was blocked with 2% lidocaine. The C7 nerve was resected at its merger points with the lateral cord and the posterior cord. After blockade with 2% lidocaine, the C7 nerve on the left side was exposed and cut as distally as possible. The C6 lamina ventrali was cut to shorten the transfer route. The anterior scalene muscle on the right side (injured side) was severed similar to the left side, and the right C7 nerve root was transected close to the intervertebral foramen. The right C7 nerve was dissected to its division level. The muscular longus colli beside the vertebral bodies was removed partially on both sides. The space between the trachea-esophagus and vertebral body was bluntly separated and expanded. Then, the C7 nerve was pulled out under the common carotid artery, the phrenic nerve, the vagus nerve, and the trachea-esophagus. It is worth noting that unlike human, the esophagus of the mouse is not behind the trachea but side by side with the trachea, on the left side of the trachea. The proximal stump of the left C7 nerve was attached to the distal stump of the right C7 nerve using 12-0 nylon sutures via the prespinal route. In accordance with CC7 surgery, the C7 nerves on both sides were exposed for the sham surgery in TBI and unlesioned groups, but only the left side C7 nerve was resected and the original brain connections of the right side C7 nerve was reserved.

BP neurotomy

Under the pentobarbital sodium anesthesia, animals were placed in the supine position. The retained BP nerves of the impaired forelimb were exposed as described above. To enlarge the operative space, the anterior scalene muscle was cut. To reserve the transferred C7 nerve alone, the C5, C6, C8, and T1 nerves were severed with microscissors, and a 1-mm segment was removed to prevent the two nerve ends spontaneous regrowth. To resect the transferred C7 nerve, a 2-mm segment (before and after neurorrhaphy site) was removed from the nerve using microscissors. The muscles and skin were sutured after the procedure.

Electrophysiological evaluation of the BP nerve

Electromyography was chosen as the method to confirm the regeneration of the transferred nerve with an electrophysiology apparatus (Dantec Keypoint G4, Natus Medicala Inc.). After mouse anesthesia, the BP nerves and the forelimb muscles were exposed via skin incision (fig. S2, A to D). A customized hooked cuff bipolar electrode (Kedou Brain-Computer Technology Co. Ltd., Suzhou, China) was placed proximal to the nerve junction site, and a wave was delivered while the recording customized needle bipolar electrode with 1 mm separation (Kedou Brain-Computer Technology Co. Ltd., Suzhou, China) was located at the target muscle belly. The CMAP amplitudes of the pectoralis major, triceps brachii, flexor, and the extensor muscles were recorded using an electric stimulus (0.5 mA with a 0.2-ms pulse). The CMAP responses were defined as a repeatable and typical two-phase curve along with visible target muscle contraction. After stimulating, the response signals were selected. The mean and SD on each time point were calculated for each mouse.

The dorsal root or ventral root cut of the C7 nerve

After anesthetizing and placing a mouse in a prone position, a 2-cm median incision was made above the T2 spinous process. The trapezius muscle and erector spinae were divided to expose C5 to T2 segments of the spinal cord (*56*). A laminectomy was performed at the left C6-C7 vertebral level, and the dura was carefully opened to expose the dorsal root of the C7 nerve. To cut the dorsal root, the sensory afferent was cut off directly using microscissors without any damage to spinal cord. To cut the ventral root, the left C5 lamina of the vertebral arch needs to be additionally removed for sufficient exposure of the spinal nerve roots. The spinal cord was pulled slightly to the right side by self-retaining retractor, and the motor efferent of the C7 nerve was resected. To prevent nerve regeneration, the nerve root was cut at two sites to leave a gap. After careful visual inspection to confirm complete resection of dorsal or ventral root of the C7 nerve, the dura mater, muscle, and skin were sutured.

Retrograde labeling of C7 nerve–mediated motor efferent and sensory afferent

The mice were anesthetized, and a midlateral incision from the cubital fossa to the midsternal line was performed to expose the BP nerve. To trace C7 nerve–mediated motor neurons and sensory neurons, about 1 μl of RV-N2C(G)-ΔG-EGFP [4×10^7 infectious units (IFU)/ml; BrainVTA, China] was injected into the middle trunk (C7 nerve) using a 5-μl Hamilton syringe (Hamilton, Bonaduz GR, Switzerland) equipped with a glass micropipette. The skin was then sutured, and the mice were perfused 5 to 7 days after the injection.

To label motor endplates in muscles of mice, Alexa Fluor 647–conjugated α-bungarotoxin (Invitrogen, B35450) was injected via the tail vein at a dose of 0.3 mg/g and a conjugation time of 1.5 hours before perfusion. The muscles of the upper arms were cut longitudinally at a depth of 300 μm from medial to lateral and cleared by three-dimensional imaging of solvent-cleared organs with superior fluorescence-preserving capability (FDISCO). Images were taken using an Olympus FV3000 confocal microscope.

AAV anterograde tracing

To achieve specific targeting of intact cortical neurons, we used a protocol described previously (*57*). Briefly, mice were anesthetized with 1.5 to 2% isoflurane and placed in a stereotaxic frame with a heated pad underneath. A scalp incision was made with eye scissors. A craniotomy (0.5 mm by 0.5 mm) was made with a dental drill. A volume of 1 μl of AAV-CaMKIIα-hChR2 (H134R)-mCherry (AAV2/9, Taitool) and AAV-CaMKIIα-hChR2 (H134R)-EYFP (AAV2/9, Taitool) was respectively injected into the RFA (1.50 mm anterior to bregma, 0.75 mm lateral to midline, and 0.8 mm ventral to skull surface) and the SFA (0.5 mm posterior to bregma, 1.75 mm lateral to midline, and 0.8 mm ventral to skull surface) of the intact cortex, using Nanoject II (Drummond Scientific) via a glass micropipette. After each injection, the micropipette was held in place for 5 to 10 min before being slowly retracted. The injection coordinates were based on the Paxios and Franklin Mouse Brain Atlas, second edition. Mice were kept for an additional 4 weeks before being sacrificed.

Retrograde trans-synaptic PRV tracing

For retrograde trans-synaptic tracing experiments, mice were anesthetized with intraperitoneal injection of 1% pentobarbital sodium and placed on a heated pad. A skin incision was made to expose the target forelimb muscles (biceps, triceps, flexors, and extensors). The muscle

was bluntly dissected carefully and separated from adjacent connective tissue. PRV-CAG-EGFP (2×10^9 PFU/ml; BrainVTA, China) was injected into the forelimb muscles (1 μl per muscle, 4 μl in total) using a 5-μl Hamilton syringe and a Hamilton needle (32 gauge, Hamilton). The skin was then sutured. Animals were kept for 5.5 days to label the intact cortical neurons, and then mice were sacrificed.

C7 spinal cord bilateral retrograde tracing

To specifically target cervical spinal cord, we used the protocol according to a previous study (*16*). The animal was anesthetized and fixed in the stereotactic frame. Then, we performed a laminectomy to expose the C7 segment of the spinal cord. On the left side, 300 nl of AAV2/2Retro-hSyn-EGFP (rAAV2, Taitool) was infused into the spinal gray matter (0.7 mm lateral and 8 mm depth) using a glass capillary, while 300 nl of AAV2/2Retro-hSyn-tdTomato (rAAV2, Taitool) was infused into the right side of the same segments. After the injection, the needle was kept in place for 5 to 10 min to prevent the backflow of the virus. Muscles and skin layers were sutured. After surgery, mice were allowed to recover for at least 4 weeks before sacrificed.

Perfusion and the transferred C7 nerve identification

All the mice were terminally anesthetized with overdose injection of pentobarbital sodium. Using a binocular microscope, it was confirmed that the right (impaired) forepaw of each mouse with crossing nerve transfer was connected to the brain via the transferred C7 nerve. The C7 nerve segments 2 mm distal and proximal to the coaptation site were collected for transmission electron microscopy. Then, animals were transcardially perfused with saline, followed by 4% phosphate-buffered paraformaldehyde solution (Servicebio). The tissues were extracted and postfixed overnight in the same solution including the brain, whole spinal cord, DRG, and the forelimb muscles. After 24 hours, the tissues were transferred to a 30% sucrose solution in phosphate-buffered saline (PBS).

Transmission electron microscopy

The distinct segments (2 mm proximal and distal to the neurorrhaphy site) were carefully dissected from the transferred C7 nerve and fixed in a 2% glutaraldehyde solution at 4°C. Then, the samples were postfixed in 1% osmium tetroxide in 0.1 M phosphate buffer for 2 hours at 4°C and embedded in Epon for 72 hours at 60°C. To enable ultrastructural observations to be made, ultrathin sections (70 nm) of the C7 transferred nerve were processed for transmission electron microscopy, negatively stained with uranyl acetate and lead citrate, and examined using a JEM-1400 transmission electron microscope (JEOL, Akishima, Tokyo, Japan). The G ratio (the ratio of the inner to the outer diameter of the myelin sheath) was used for evaluating the regeneration of the transferred C7 nerve, according to previous studies (*58*).

Histology and immunohistochemistry

After embedding into optimal cutting temperature compound, the samples were snap-frozen in dry ice. Serial coronal sections (40 μm) were collected and stored at −20°C until processed. To assess the extent of intact CST sprouting, serial sections of the spinal cords were cut in the transverse plane. Besides, spinal cords, DRGs, and muscles of the forelimb were cut at a depth of 15 to 40 μm and mounted in adhesive slides (Thermo Fisher Scientific) to label sensory afferent or motor efferent of the transferred C7 nerve. Primary antibodies used in immunohistochemistry were rabbit anti-parvalbumin (1:500; Abcam, catalog no. ab256811), guinea pig anti-vesicular glutamate transporter 1 (1:1000; Synaptic Systems, catalog no. 135 304), goat anti–choline acetyltransferase (1:500; Millipore, catalog no. AB144P), goat anti-calcitonin gene related peptide (1:500; Abcam, catalog no. ab36001), goat anti-GFP (1:1000; Abcam, catalog no. ab6673), rabbit anti-GFP (1:1000; Thermo Fisher Scientific, catalog no. A11122), and rabbit anti-DsRed (1:500; Clontech, catalog no. 632496). Secondary antibodies were donkey anti-goat immunoglobulin G (IgG)–Alexa Fluor 488 (1:500; Jackson ImmunoResearch Laboratories), donkey anti-rabbit IgG–Alexa Fluor 488 (1:500; Jackson ImmunoResearch Laboratories), donkey anti-rabbit IgG-Cy3 (1:500; Jackson ImmunoResearch Laboratories), donkey anti-guinea pig IgG–Alexa Fluor 647 (1:500; Jackson ImmunoResearch Laboratories), and donkey anti-goat IgG–Alexa Fluor 647 (1:500; Invitrogen). 4′,6-Diamidino-2-phenylindole (1:500; Roche) was used for nuclei staining. Images were taken using an Olympus VS120 fluorescence microscope, an Olympus FV3000 microscope, or a Nikon TiE-A1 Plus confocal microscope. Cell counting was carried out manually or automatically using Fiji [National Institutes of Health (NIH)].

Quantification of C7 nerve–mediated sensory afferent or motor efferent

To define the percentage of positive signals for immunostaining in DRG neurons labeled by RV, we performed quantification analysis according to methods described in detail previously (*23*). After setting the intensity threshold, the immunoreactivity signals were clustered into positive (above threshold) or negative (below threshold) group. The DRG neurons with positive signals were counted, and the percentage of RV positive DRG neurons expressing PV or CGRP was quantified manually by Fiji (NIH). The method of analyzing the colocalization of CGRP/VGLUT1 and sensory afferent labeled by RV in the spinal cord was by following the previously published procedure (*59*). Briefly, high-magnification confocal images of laminae 1 to 5 with single Z-section were assessed using the Otsu thresholding method in Fiji. After threshold subtraction, RV-, VGLUT1-, and CGRP-marked regions were depicted and quantified.

The fraction of non-, partially, and fully reinnervated NMJ was counted in Z-stack confocal microscopy images. The innervation status of individual NMJ was classified according to the extent to which the RV labeling overlaid with α-bungarotoxin staining and was presented as relative to 100% [referent to a tissue where all NMJs are completely innervated (full innervated)]. No innervated NMJs were devoid of any RV labeling. Partially innervated NMJs were identified as only part of the α-bungarotoxin–positive endplates being covered by RV labeling. For each muscle sample, at least 20 NMJs were evaluated from randomly selected visual fields.

Quantification of PRV retrograde tracing

All the labeled cortical neurons were manually counted on each layer using Lunion BNS 2020 (www.luniondata.com) and measured coordinates of each cell together with the landmark specifications exported. The brain size was normalized to a template, and brain midline was straightened by means of defined anatomical landmarks and trigonometric calculations. Cell numbers were use-normalized by KDE (kernel density estimation). KDE is a nonparametric way to estimate the probability density function of a random variable. KDE is a fundamental data smoothing problem where inferences about the population are made on the basis of a finite data sample. All data and their heatmap charts using KDE are extracted using customized in Lunion BNS 2020.

Quantification of CST axon number and fluorescence intensity

In the subcortical brain image, the mapping of S1 output projections was performed as previously described (*60*). After aligning these brain slices to the corresponding sections of the Allen Mouse Brain Atlas (2015 Allen Institute for Brain Science, Allen Brain Atlas API, available at brain-map.org/api/index.html) based on several reference points, we chose an appropriate threshold to binarize these images while preserving the real fluorescent signal as much as possible. The relative fluorescence intensities were normalized to that of the cortical area injected with AAV-ChR2-EYFP. In the spinal cord images, densitometry measurement on each side of the gray matter was taken using MetaMorph software, after being subthreshold to the background and normalized by area. Densities were calculated within each region of interest (ROI) as the ratio of labeled fibers (number of pixels) per ROI area (*20*). The relative fluorescence intensities in the spinal cord were the ratio of the fluorescence intensities of axons in the affected spinal cord to the contralateral spinal cord. QuPath was used to calculate the mean fluorescence intensities of axons (*61*). The outcome measure of the sprouting axon number index was the ratio of contralateral and ipsilateral counts. To quantify the number of sprouting axons, we followed the methods used in a previous study (*32*). Briefly, we drew a horizontal line through the central canal and across the lateral rim of the gray matter. Three vertical lines (mid, Z1, and Z2, and we defined Z1′ and Z2′ in the relative position of the opposite side) were then drawn to divide the horizontal line into three equal parts, starting from the central canal to the lateral rim. Only axons crossing the three lines were counted in each section. For CST axons in the spinal cord, at least three sections from the spinal cord C5 to T1 were selected per animal.

In vivo wide-field Ca^{2+} imaging

As reported previously, *Thy1-GCamp6s* mice were anesthetized with 0.5 to 1.0% isoflurane in oxygen (*62*). Animals were placed in a stereotactic frame and kept at a stable depth of anesthesia, characterized by loss of reflexes and a respiratory rate of 100 to 120 breaths/min. Rectal temperature was monitored and maintained at 38°C using a heating pad throughout the experiments. The skull at the sensorimotor cortex was exposed and covered with a 3-mm window. Cortical images (pixels) of green (l = 500 to 550 nm) fluorescence in blue (l = 450 to 490 nm) excitation light were recorded using a cooled charge-coupled device camera system (Retiga R1, Telendye Photometrics). The camera was attached to a binocular epifluorescence microscope (H157, Prior Scientific) with an objective lens (Olympus MPLN4X).

Electrical stimulation was applied to the forepaw by inserting stimulation electrodes (Roboz) both on the proximal site of the wrist and palm. Electrical stimulation was provided in a block design (model 2100, A-M Systems) with the following parameters: 20-s rest, 1-s stimulation (0.6 mA, 5-ms duration), and 39-s rest as previously described in other remapping studies. Then, the cortex was positioned in focus of the camera, and the animals were then transitioned to isoflurane anesthesia (<0.5%) for stimulation studies.

Fluorescence images were obtained at 10 frames/s, which were averaged over 10 trials. The images were shown in a pseudo-color scale in terms of relative fluorescence changes ($\Delta F/F_0$), which were obtained by dividing increased in fluorescence intensity (ΔF) in each pixel by averaged intensity in 20 frames immediately before stimulation (F_0). Response amplitude was evaluated as $\Delta F/F_0$ at each pixel position. The response peak frame has the highest mean response amplitude averaged over all pixel positions. A threshold (0.15) was set for response amplitude $\Delta F/F_0$ at all pixel positions of the peak amplitude frame. Response amplitudes larger than the threshold were considered as responded to the stimulus at corresponding pixel positions.

Custom-written Python programs were used to analyze and quantify the Ca^{2+} signals (peak amplitude, time to peak amplitude, and area under the curve) in ROIs. On the basis of Allen Mouse Brain Atlas (Allen Brain Atlas API, available at brain-map.org/api/index.html), two circle ROIs in M1 (center at ML = 1.25 mm, AP = 0.25 mm, and d = 0.5 mm) and S1 (center at ML = 2.0 mm, AP = −0.5 mm, and d = 0.5 mm) were defined to quantify the variation tendency of the Ca^{2+} signals. Peak amplitude was calculated by finding the maximum response in the first 4000 ms after stimulus in the trial averaged percentage $\Delta F/F_0$. Time-to-peak amplitude is the difference in time of the stimulus and the response peak frame. Area under curve was calculated by the summation of response amplitude of 10 frames (1 s) after the stimulus.

Behavioral analysis

Single-pellet reaching test

The single-pellet reaching test estimates accurate use the forelimb (right) when grabbing the single pellet (*63*). Mice were placed in a transparent plexiglass chamber of 20 cm by 8.5 cm by 15 cm dimension and 1 mm in thickness, on the middle part of the front wall of the chamber was located a vertical slit (5 mm wide; 13 cm high). Single pellets were located on a platform outside the slit. The whole process of the retrieval of each mouse was recorded with a video camera on the front and side. Reaching accuracy was classified with slow motion video surveillance according to four categories: miss (i, no contact with the pellet during reach), no grasp (ii, paw contact with pellet but no correct grasping), drop (iii, the pellet is retrieved but falls before taking it into the mouth), success (All, the mouse retrieves the pellet directly to its mouth). The number of times in each category was determined manually. A total of 20 successful grasps (All) were counted during each session. This test requires pretraining and food deprivation, mice with baseline success rate lower than 30% were excluded from analysis. Success rate was calculated as the percentage of successful reaches over total reaching attempts. The metacarpophalangeal joint of paws was traced manually from the moment the paw is lifted from the ground until it touches the pellet to measure the trajectory of paws. Custom-written Python programs were used to plot the images of trajectory and analyze the height and the Harsdorff distance.

Cylinder test

The cylinder test evaluates forelimb use during spontaneous vertical exploration within a cylinder (*64*, *65*). Mice were placed in a transparent cylinder (diameter of 9 cm, height of 15 cm) on an elevated frame. To facilitate observing and recording, a mirror was fixed at a 45° angle below the cylinder. Spontaneous rearing of each mouse in the mirror was videotaped for 5 min. The amount of time (seconds) that is spent on either the right paw, left paw, or both paws that made contact with the glass walls was determined manually. Only rears in which both forelimbs could be clearly seen were timed. Mice not active during the test were excluded from analysis. The percentage of time spent on each limb was calculated, and these data were used to derive an asymmetry index (% left paw contact time – % right paw contact time).

Grid-walking test

The grid-walking test assesses the ability to accurately place the forepaws on the rungs of a grid during spontaneous exploration (*64*, *65*).

Mice were placed on a wire grid (20 cm by 24 cm) with 25-mm square holes and allowed to freely explore for a period 10 min while performance was recorded with a video camera. A foot slip was scored when the paw completely missed a rung (in which case the limb fell between rungs and the animal lost balance) or when the paw was correctly placed on a rung but slipped off while bearing body weight. The total number of foot slip for each limb, along with the total number of nonslip steps, was counted, and the ratio between foot slips and total-steps-taken was calculated. Percent foot slips of the right forelimb were calculated by [foot slips/(foot slips + on-slip steps) × 100]. Neither the cylinder test nor the grid-walk test requires training.

Open-field test

Different parameters of animal motion were quantified using an overhead camera and Noldus Ethovision XT 13 software (Leesburg, VA). Mice were placed in a square plexiglass chamber of 40 cm by 40 cm by 40 cm dimension at the same border, and behavior such as moving, crossings, rearing, and grooming was recorded during free movement for 10 min. The center area was defined as centric 20 cm by 20 cm. Analysis of total distance and duration of movement were conducted using Noldus Ethovision XT 13, and velocity was calculated by dividing the total distance with duration for moving. The seconds before the first entry to the center square, the numbers of fecal particles, the times of grooming, and border square duration were recorded as an index of exploration and anxiety activities.

Rotarod test

On the first 2 days, mice were placed on a rotarod apparatus (Ugo Basile, Italy) that accelerated 5 to 20 rpm for 5 min and were trained to maintain their balancing walking. On the third day, rod accelerated 5 to 40 rpm, and mice were tested with a maximum time of 300 s. The latencies of animals to fall off were recorded. All behavioral testing and analysis were done by an observer blinded to the experimental groups.

Optogenetic cortical stimulation and EMG recording

Optogenetic cortical stimulation and EMG recording were conducted as previously reported (*20*). *Thy1-ChR2* mice were anesthetized with 0.5 to 1.0% isoflurane in oxygen and placed in a stereotaxic frame with a heated pad underneath. Animals were kept at a stable depth of anesthesia, characterized by loss of reflexes and a respiratory rate of 100 to 120 breaths/min. A scalp incision was made with eye scissors. The skull was opened with a surgical drill (approximately a rectangle, ML = 0 to 2.75 mm and AP = −1.25 to 2.25 mm), and the sensorimotor region of the cortex was exposed. Light stimulation was provided by a 473-nm 4-mW laser (Shanghai Laser and Optics Century Co. Ltd., China) targeted to the brain through an optical fiber (fiber core = 200 μm, numerical aperture = 0.22, depth = 3 mm). The laser stimulations were controlled by a Master-9 pulse stimulator (AMPI, Israel). A grid of 5 × 7 stimulation points spaced 500 μm apart was superimposed on an image of the cortex, and a 5-ms light pulse was delivered to each point in a random order. Laser power was measured at the plane of the brain surface with a power meter (Sanwa Electric Instrument Co. Ltd., Japan). We recorded EMG responses of the bilateral triceps muscle using two 250-μm-diameter 304 stainless steel electrode with 1-mm separation (Kedou Brain-Computer Technology Co. Ltd., Suzhou, China) with a separate ground, in response to stimulation of intact cortical neurons. EMG responses were recorded (24 bits at 1 KHz) using an electrophysiology data acquisition system (Medusa, Bio-Signal Technologies, China/USA). EMG signals were extracted with a 50-Hz filter and then stored for further analysis.

To identify the innervation of contralesional SFA to the impaired forelimb, the AAV-CaMKIIα-hChR2 (H134R)-EYFP (AAV2/9, Taitool) were injected into the SFA (0.5 mm posterior to bregma, 1.75 mm lateral to midline, and 0.8 mm ventral to skull surface) of the intact cortex. After 4 weeks, the animals were subjected to optical stimulation experiments with anesthesia and craniotomy as described above. The same light stimulation was targeted to the central point of SFA. EMG responses of the bilateral triceps brachii, biceps brachii, forearm extensor muscle, and forearm flexor muscle were recorded and processed as described above.

Custom-written Python programs were used to analyze and quantify the EMG signal. Three times the SD of the 2-s signal before every laser stimulation was defined as a threshold. Signals that exceed the threshold in 500 ms after stimulation were considered as responses. The maximum response current divided by its threshold was accumulated as the response index. According to the positions of the stimulation point, the 35 rectangle regions were divided into M2 (8 points), M1 (10 points), and S1 (16 points) based on Allen Mouse Brain Atlas (Allen Brain Atlas API, available at brain-map.org/api/index.html) and RFA (3 points) and CFA (10 points) based on previous studies (*15*, *18*, *66*).

RNA sequencing

Bulk RNA-seq

RNA-seq was performed using RNA from sensorimotor cortex tissue in five biological replicates. The cortex was extracted and stored in RNAlater (Qiagen). According to manufacturer's protocol, cortex tissue's RNA was extracted by an RNAeasy kit (Qiagen). RNA concentrations and quality were measured using the RNA Nano 6000 Assay Kit of the Bioanalyzer 2100 system (Agilent Technologies, CA, USA). A total amount of 1 μg of RNA per sample was used as input material for library preparation. Libraries were generated using the NEBNext UltraTM RNA Library Prep Kit for Illumina (New England Biolabs, USA) following the manufacturer's recommendations, and index codes were added to attribute sequences to each sample. The library preparations were sequenced on an Illumina NovaSeq platform, and 150-bp paired-end reads were generated. After removing reads containing adapter, reads containing ploy-N, and low-quality reads from raw data, paired-end clean reads were aligned to the GRCm38 (mm10) mouse reference genome sequence using Hisat2 v2.0.5. featureCounts v1.5.0-p3 was used to count the read numbers mapped to each gene, and then fragments per kilobase million (FPKM) of each gene was calculated on the basis of the length of the gene and reads count mapped to this gene. EdgeR R package (3.18.1) was used to identify DEGs. The heatmap of RNA-seq mRNA expression levels of the differential expression genes in any sample group ($P < 0.05$) was generated by Euclidean unsupervised hierarchical clustering in RStudio (1.3.1073) using the ggplot2.

GO analysis

GO analysis of up-regulated or down-regulated marker genes in specific cell clusters or whole transcriptome in TBI + CC7, TBI + sham, and unlesioned mice were implemented by the clusterProfiler R package using a threshold of $P < 0.05$, in which gene length bias was corrected. Functional GO clustering was performed using ClueGO in Cytoscape (http://cytoscape.org): (Bonferroni $P < 0.05$) (GO tree interval, minimum of 5 and maximum 8) (GO selection, minimum of 10; 5%) (*K* score of 0.4) (*23*).

Molecular pathway analysis

The network was made by ingenuity pathway analysis, where each node represents a DEG (RNA-seq), and solid lines between nodes indicate direct interactions and dashed lines indicate indirect interactions.

snRNA-seq tissue dissociation

The cortex was extracted and stored in RNase later (Qiagen). Sensorimotor cortex tissues were transported in a sterile culture dish with 10 ml of 1× Dulbecco's PBS (Thermo Fisher Scientific) on ice to remove the residual tissue storage solution, and then nuclei were isolated using a Dounce homogenizer (VWAR, Batavia, IL, USA) in RNase-free lysis buffer (Boyou), followed by lysis at 4°C for 10 min. The samples were centrifuged at 500*g* for 5 min. We removed the supernatant and resuspended the nuclei in 1 ml of resuspension buffer. Nuclei suspensions were filtered using a 40-μm nylon cell strainer, then centrifuged, and resuspended again. Nuclei were stained with 0.4% trypan blue (Thermo Fisher Scientific) to check the viability on Countess II Automated Cell Counter (Thermo Fisher Scientific). Cell nuclei were prepared from cortical tissues of three different mice for both TBI + CC7 and TBI + sham groups.

10× library preparation and sequencing

Beads with unique molecular identifier (UMI) and cell barcodes were loaded close to saturation, so that each cell was paired with a bead in a gel beads–in–emulsion. The library constructions were performed according to the standard manufacturer's protocol (CG000206 RevD). Sequencing libraries were quantified using a High Sensitivity DNA Chip (Agilent) on a Bioanalyzer 2100 and the Qubit High Sensitivity DNA Assay (Thermo Fisher Scientific). The libraries were sequenced on NovaSeq6000 (Illumina) using 2x150 chemistry.

snRNA-seq data processing

Reads were processed using the Cell Ranger 2.1.0 pipeline with default and recommended parameters. FASTQs generated from Illumina sequencing output were aligned to the mouse genome, version GRCm38, using the STAR algorithm. Next, gene-barcode matrices were generated for each individual sample by counting UMIs and filtering noncell-associated barcodes. Last, we generate a gene-barcode matrix containing the barcoded cells and gene expression counts. This output was then imported into the Seurat (v2.3.0) R toolkit for quality control and downstream analysis of our single-cell RNA-seq data (*67*). We excluded cells with fewer than 200 or more than 6000 detected genes (where each gene had to have at least one UMI aligned in at least three cells). The expression of mitochondria genes was calculated (*67*). To remove low activity cells, cells with more than 10% expression of mitochondria genes were excluded. The normalized data were performed for extracting a subset of variable genes. Variable genes were identified while controlling for the strong relationship between variability and average expression. Next, we integrated data from different samples after identifying "anchors" between datasets (*67*, *68*). Then, we performed principal components analysis (PCA) and reduced the data to the top 30 PCA components after scaling the data. We visualized the clusters on a two-dimensional map produced with *t*-distributed stochastic neighbor embedding (t-SNE) (*69*).

Identification of cell types and subtypes by nonlinear dimensional reduction (t-SNE)

Cells were clustered using graph-based clustering of the PCA reduced data with the Louvain method after computing a shared nearest neighbor graph (*67*). For subclustering, we applied the same procedure of scaling, dimensionality reduction, and clustering to the specific set of data (usually restricted to one type of cell). For each cluster, we used the Wilcoxon rank-sum test to find significant DEGs comparing the remaining clusters. SingleR (*70*) and known marker genes were used to identify cell type.

Pharmacogenetic inhibition of the ipsiCSNs

To selectively express hM4Di in CSNs from the intact cortex to the impaired spinal cord, we applied a Cre-dependent approach (*41*). At 8 weeks after CC7 surgery, animals were injected with 1 μl of AAV-hSyn-DIO-hM4D(Gi)-mCherry (AAV2/9, Taitool) in the intact sensory cortex, followed by injection of 300 nl of retro-AAV-hSyn-Cre (rAAV2, Taitool) in the spinal cord of the impaired side at C5-C6 segments and C7-C8 segments, respectively. In the control animal, the spinal cord of the impaired side received injections of retro AAV-hSyn-GFP (rAAV2, Taitool), and the intact sensory cortex also received the injection of 1 μl of AAV-hSyn-DIO-hM4D(Gi)-mCherry (AAV2/9, Taitool). Clozapine-*N*-oxide (CNO, Sigma-Aldrich) or saline was then administered (1 mg/kg, ip) 4 weeks after virus injection, in which the skilled motor function of impaired forelimb was almost completely recovered. Then, the mice were tested for the single-pellet reaching test, the cylinder test, and the grid-walking test to reassess their performance of the skilled forelimb function.

Electrophysiological slice recording

Slice electrophysiology was performed as described previously (*57*). Mice were anesthetized and perfused transcardially with an ice-cold cutting solution containing 213 mM sucrose, 2.5 mM KCl, 1.25 mM NaH_2PO_4, 10 mM $MgSO_4$, 0.5 mM $CaCl_2$, 26 mM $NaHCO_3$, and 11 mM glucose (300 to 305 mOsm). The brain was rapidly dissected, and coronal slices (220 μm) were sectioned in the ice-cold cutting solution, using a vibratome (Leica VT1200S) at slicing speeds of 0.12 mm/s and a blade vibration amplitude of 1 mm. Slices were transferred to the holding chamber and incubated in 34°C artificial cerebral spinal fluid (ACSF) containing 126 mM NaCl, 2.5 mM KCl, 1.25 mM NaH_2PO_4, 2 mM $MgCl_2$, 2 mM $CaCl_2$, 26 mM $NaHCO_3$, and 10 mM glucose (300 to 305 mOsm) to recover for 30 min. The slices were then kept at room temperature before recordings. Both cutting solution and ACSF were continuously bubbled with 95% O_2/5% CO_2.

Slices were placed on glass coverslips coated with poly-L-lysine (Sigma-Aldrich, St. Louis, MO) and submerged in a recording chamber (Warner Instruments, Hamden, CT) while perfusing the recording chamber with ACSF at 3 ml/min using a pump (HL-2, Shanghai Huxi). In designer receptor exclusively activated by a designer drug (DREADD) experiments, $hM4Di^+$ neurons in the sensory cortex were recorded in whole-cell configuration, and CNO (5 μM) was bath-applied. Whole-cell recordings were obtained with pipettes (3 to 5 megohm) filled with potassium-based internal solution containing 130 mM K-gluconate, 1 mM $MgCl_2$, 1 mM $CaCl_2$, 1 mM KCl, 10 mM Hepes, 11 mM EGTA, 2 mM Mg–adenosine 5′-triphosphate, 0.3 mM Na–guanosine 5′-triphosphate (pH 7.3, 290 mOsm). Recording was performed in current-clamp mode, a current of 100 pA was injected into the recorded neurons, and the evoked voltage change was recorded under normal and CNO conditions. Stimulus delivery and the data acquisition were conducted with a multiclamp 700B amplifier and Digidata 1440A (Molecular Devices), which were controlled by Clampex 10.2 (Molecular Devices). The data were analyzed by Clampfit10.4. All chemicals were obtained from Sigma-Aldrich, unless otherwise noted.

Statistical analysis

The primary outcome experimental parameter for skilled motor functional testing was the success rate of the impaired forelimb in the single-pellet reaching task. The secondary outcomes were foot faults of the impaired forelimb in grid-walking test and limb-use asymmetry in the cylinder test. Data are presented as means ± SEM. The distribution of the variables in each experimental group was assumed to be normal. Statistical analysis was performed using Igor Pro (Wavemetrics) and Prism 8 (GraphPad Software). All statistical analyses were two-tailed comparisons. No statistical method was used to predetermine the sample size; however, the sample sizes were similar to those generally used in the field (*32*, *42*, *63*). All data met the assumptions of the statistical tests used. The data were analyzed using unpaired *t* test, Wilcoxon signed-rank test, and two-way analysis of variance (ANOVA), followed by Bonferroni post hoc test.

SUPPLEMENTARY MATERIALS

Supplementary material for this article is available at https://science.org/doi/10.1126/sciadv.abn5899

REFERENCES AND NOTES

1. V. L. Feigin, E. Nichols, T. Alam, M. S. Bannick, E. Beghi, N. Blake, W. J. Culpepper, E. R. Dorsey, A. Elbaz, R. G. Ellenbogen, J. L. Fisher, C. Fitzmaurice, G. Giussani, L. Glennie, S. L. James, C. O. Johnson, N. J. Kassebaum, G. Logroscino, B. Marin, W. C. Mountjoy-Venning, M. Nguyen, R. Ofori-Asenso, A. P. Patel, M. Piccininni, G. A. Roth, T. J. Steiner, L. J. Stovner, C. E. I. Szoeke, A. Theadom, S. E. Vollset, M. T. Wallin, C. Wright, J. R. Zunt, N. Abbasi, F. Abd-Allah, A. Abdelalim, I. Abdollahpour, V. Aboyans, H. N. Abraha, D. Acharya, A. A. Adamu, O. M. Adebayo, A. M. Adeoye, J. C. Adsuar, M. Afarideh, S. Agrawal, A. Ahmadi, M. B. Ahmed, A. N. Aichour, I. Aichour, M. T. E. Aichour, R. O. Akinyemi, N. Akseer, A. al-Eyadhy, R. al-Shahi Salman, F. Alahdab, K. A. Alene, S. M. Aljunid, K. Altirkawi, N. Alvis-Guzman, N. H. Anber, C. A. T. Antonio, J. Arabloo, O. Aremu, J. Ärnlöv, H. Asayesh, R. J. Asghar, H. T. Atalay, A. Awasthi, B. P. Ayala Quintanilla, T. B. Ayuk, A. Badawi, M. Banach, J. A. M. Banoub, M. A. Barboza, S. L. Barker-Collo, T. W. Bärnighausen, B. T. Baune, N. Bedi, M. Behzadifar, M. Behzadifar, Y. Béjot, B. B. Bekele, A. B. Belachew, D. A. Bennett, I. M. Bensenor, A. Berhane, M. Beuran, K. Bhattacharyya, Z. A. Bhutta, B. Biadgo, A. Bijani, N. Bililign, M. S. Bin Sayeed, C. K. Blazes, C. Brayne, Z. A. Butt, I. R. Campos-Nonato, C. Cantu-Brito, M. Car, R. Cárdenas, J. J. Carrero, F. Carvalho, C. A. Castañeda-Orjuela, F. Castro, F. Catalá-López, E. Cerin, Y. Chaiah, J. C. Chang, I. Chatziralli, P. P. C. Chiang, H. Christensen, D. J. Christopher, C. Cooper, P. A. Cortesi, V. M. Costa, M. H. Criqui, C. S. Crowe, A. A. M. Damasceno, A. Daryani, V. de la Cruz-Góngora, F. P. de la Hoz, D. de Leo, G. T. Demoz, K. Deribe, S. D. Dharmaratne, D. Diaz, M. T. Dinberu, S. Djalalinia, D. T. Doku, M. Dubey, E. Dubljanin, E. E. Duken, D. Edvardsson, Z. el-Khatib, M. Endres, A. Y. Endries, S. Eskandarieh, A. Esteghamati, S. Esteghamati, F. Farhadi, A. Faro, F. Farzadfar, M. H. Farzaei, B. Fatima, S. M. Fereshtehnejad, E. Fernandes, G. T. Feyissa, I. Filip, F. Fischer, T. Fukumoto, M. Ganji, F. G. Gankpe, M. A. Garcia-Gordillo, A. K. Gebre, T. G. Gebremichael, B. K. Gelaw, J. M. Geleijnse, D. Geremew, K. E. Gezae, M. Ghasemi-Kasman, M. Y. Gidey, P. S. Gill, T. K. Gill, E. T. Girma, E. V. Gnedovskaya, A. C. Goulart, A. Grada, G. Grosso, Y. Guo, R. Gupta, R. Gupta, J. A. Haagsma, T. B. Hagos, A. Haj-Mirzaian, A. Haj-Mirzaian, R. R. Hamadeh, S. Hamidi, G. J. Hankey, Y. Hao, J. M. Haro, H. Hassankhani, H. Y. Hassen, R. Havmoeller, S. I. Hay, M. I. Hegazy, B. Heidari, A. Henok, F. Heydarpour, C. L. Hoang, M. K. Hole, E. Homaie Rad, S. M. Hosseini, G. Hu, E. U. Igumbor, O. S. Ilesanmi, S. S. N. Irvani, S. M. S. Islam, M. Jakovljevic, M. Javanbakht, R. P. Jha, Y. B. Jobanputra, J. B. Jonas, J. J. Jozwiak, M. Jürisson, A. Kahsay, R. Kalani, Y. Kalkonde, T. A. Kamil, T. Kanchan, M. Karami, A. Karch, N. Karimi, A. Kasaeian, T. D. Kassa, Z. Y. Kassa, A. Kaul, A. T. Kefale, P. N. Keiyoro, Y. S. Khader, M. A. Khafaie, I. A. Khalil, E. A. Khan, Y. H. Khang, H. Khazaie, A. A. Kiadaliri, D. N. Kiirithio, A. S. Kim, D. Kim, Y. E. Kim, Y. J. Kim, A. Kisa, Y. Kokubo, A. Koyanagi, R. V. Krishnamurthi, B. Kuate Defo, B. Kucuk Bicer, M. Kumar, B. Lacey, A. Lafranconi, V. C. Lansingh, A. Latifi, C. T. Leshargie, S. Li, Y. Liao, S. Linn, W. D. Lo, J. C. F. Lopez, S. Lorkowski, P. A. Lotufo, R. M. Lucas, R. Lunevicius, M. T. Mackay, N. B. Mahotra, M. Majdan, R. Majdzadeh, A. Majeed, R. Malekzadeh, D. C. Malta, N. Manafi, M. A. Mansournia, L. G. Mantovani, W. März, T. P. Mashamba-Thompson, B. B. Massenburg, K. K. V. Mate, C. McAlinden, J. J. McGrath, V. Mehta, T. Meier, H. G. Meles, A. Melese, P. T. N. Memiah, Z. A. Memish, W. Mendoza, D. T. Mengistu, G. Mengistu, A. Meretoja, T. J. Meretoja, T. Mestrovic, B. Miazgowski, T. Miazgowski, T. R. Miller, G. K. Mini, E. M. Mirrakhimov, B. Moazen, B. Mohajer, N. Mohammad Gholi Mezerji, M. Mohammadi, M. Mohammadi-Khanaposhtani, R. Mohammadibakhsh, M. Mohammadnia-Afrouzi, S. Mohammed, F. Mohebi, A. H. Mokdad, L. Monasta, S. Mondello, Y. Moodley, M. Moosazadeh, G. Moradi, M. Moradi-Lakeh, M. Moradinazar, P. Moraga, I. Moreno Velásquez, S. D. Morrison, S. M. Mousavi, O. S. Muhammed, W. Muruet, K. I. Musa, G. Mustafa, M. Naderi, G. Nagel, A. Naheed, G. Naik, F. Najafi, V. Nangia, I. Negoi, R. I. Negoi, C. R. J. Newton, J. W. Ngunjiri, C. T. Nguyen, L. H. Nguyen, D. N. A. Ningrum, Y. L. Nirayo, M. R. Nixon, B. Norrving, J. J. Noubiap, M. Nourollahpour Shiadeh, P. S. Nyasulu, O. S. Ogah, I. H. Oh, A. T. Olagunju, T. O. Olagunju, P. R. Olivares, O. E. Onwujekwe, E. Oren, M. O. Owolabi, M. PA, A. H. Pakpour, W. H. Pan, S. Panda-Jonas, J. D. Pandian, S. K. Patel, D. M. Pereira, M. Petzold, J. D. Pillay, M. A. Piradov, G. V. Polanczyk, S. Polinder, M. J. Postma, R. Poulton, H. Poustchi, S. Prakash, V. Prakash, M. Qorbani, A. Radfar, A. Rafay, A. Rafiei, F. Rahim, V. Rahimi-Movaghar, M. Rahman, M. H. U. Rahman, M. A. Rahman, F. Rajati, U. Ram, A. Ranta, D. L. Rawaf, S. Rawaf, N. Reinig, C. Reis, A. M. N. Renzaho, S. Resnikoff, S. Rezaeian, M. S. Rezai, C. M. Rios González, N. L. S. Roberts, L. Roever, L. Ronfani, E. M. Roro, G. Roshandel, A. Rostami, P. Sabbagh, R. L. Sacco, P. S. Sachdev, B. Saddik, H. Safari, R. Safari-Faramani, S. Safi, S. Safiri, R. Sagar, R. Sahathevan, A. Sahebkar, M. A. Sahraian, P. Salamati, S. Salehi Zahabi, Y. Salimi, A. M. Samy, J. Sanabria, I. S. Santos, M. M. Santric Milicevic, N. Sarrafzadegan, B. Sartorius, S. Sarvi, B. Sathian, M. Satpathy, A. R. Sawant, M. Sawhney, I. J. C. Schneider, B. Schöttker, D. C. Schwebel, S. Seedat, S. G. Sepanlou, H. Shabaninejad, A. Shafieesabet, M. A. Shaikh, R. A. Shakir, M. shams-Beyranvand, M. shamsizadeh, M. Sharif, M. Sharif-Alhoseini, J. She, A. Sheikh, K. N. Sheth, M. Shigematsu, R. Shiri, R. Shirkoohi, I. Shiue, S. Siabani, T. J. Siddiqi, I. D. Sigfusdottir, R. Sigurvinsdottir, D. H. Silberberg, J. P. Silva, D. G. A. Silveira, J. A. Singh, D. N. Sinha, E. Skiadaresi, M. Smith, B. H. Sobaih, S. Sobhani, M. Soofi, I. N. Soyiri, L. A. Sposato, D. J. Stein, M. B. Stein, M. A. Stokes, M.'. B. Sufiyan, B. L. Sykes, P. N. Sylaja, R. Tabarés-Seisdedos, B. J. te Ao, A. Tehrani-Banihashemi, M. H. Temsah, O. Temsah, J. S. Thakur, A. G. Thrift, R. Topor-Madry, M. Tortajada-Girbés, M. R. Tovani-Palone, B. X. Tran, K. B. Tran, T. C. Truelsen, A. G. Tsadik, L. Tudor Car, K. N. Ukwaja, I. Ullah, M. S. Usman, O. A. Uthman, P. R. Valdez, T. J. Vasankari, R. Vasanthan, Y. Veisani, N. Venketasubramanian, F. S. Violante, V. Vlassov, K. Vosoughi, G. T. Vu, I. S. Vujcic, F. S. Wagnew, Y. Waheed, Y. P. Wang, E. Weiderpass, J. Weiss, H. A. Whiteford, T. Wijeratne, A. S. Winkler, C. S. Wiysonge, C. D. A. Wolfe, G. Xu, A. Yadollahpour, T. Yamada, Y. Yano, M. Yaseri, H. Yatsuya, E. M. Yimer, P. Yip, E. Yisma, N. Yonemoto, M. Yousefifard, C. Yu, Z. Zaidi, S. B. Zaman, M. Zamani, H. Zandian, Z. Zare, Y. Zhang, S. Zodpey, M. Naghavi, C. J. L. Murray, T. Vos, Global, regional, and national burden of neurological disorders, 1990–2016: A systematic analysis for the Global Burden of Disease Study 2016. *Lancet Neurol.* **18**, 459–480 (2019).
2. P. Lu, Y. Wang, L. Graham, K. McHale, M. Gao, D. Wu, J. Brock, A. Blesch, E. S. Rosenzweig, L. A. Havton, B. Zheng, J. M. Conner, M. Marsala, M. H. Tuszynski, Long-distance growth and connectivity of neural stem cells after severe spinal cord injury. *Cell* **150**, 1264–1273 (2012).
3. H. Nakatomi, T. Kuriu, S. Okabe, S. I. Yamamoto, O. Hatano, N. Kawahara, A. Tamura, T. Kirino, M. Nakafuku, Regeneration of hippocampal pyramidal neurons after ischemic brain injury by recruitment of endogenous neural progenitors. *Cell* **110**, 429–441 (2002).
4. G. Di Pino, G. Pellegrino, G. Assenza, F. Capone, F. Ferreri, D. Formica, F. Ranieri, M. Tombini, U. Ziemann, J. C. Rothwell, V. D. Lazzaro, Modulation of brain plasticity in stroke: A novel model for neurorehabilitation. *Nat. Rev. Neurol.* **10**, 597–608 (2014).
5. M. T. Joy, E. B. Assayag, D. Shabashov-Stone, S. Liraz-Zaltsman, J. Mazzitelli, M. Arenas, N. Abduljawad, E. Kliper, A. D. Korczyn, N. S. Thareja, E. L. Kesner, M. Zhou, S. Huang, T. K. Silva, N. Katz, N. M. Bornstein, A. J. Silva, E. Shohami, S. T. Carmichael, CCR5 is a therapeutic target for recovery after stroke and traumatic brain injury. *Cell* **176**, 1143–1157.e13 (2019).
6. G. Kwakkel, J. M. Veerbeek, E. E. van Wegen, S. L. Wolf, Constraint-induced movement therapy after stroke. *Lancet Neurol.* **14**, 224–234 (2015).
7. M. X. Zheng, X. Y. Hua, J. T. Feng, T. Li, Y. C. Lu, Y. D. Shen, X. H. Cao, N. Q. Zhao, J. Y. Lyu, J. G. Xu, Y. D. Gu, W. D. Xu, Trial of contralateral seventh cervical nerve transfer for spastic arm paralysis. *N. Engl. J. Med.* **378**, 22–34 (2018).
8. S. Brown, The brain power of man. *Am. J. Dent. Sci.* **8**, 82–87 (1874).
9. B. Gesslbauer, L. A. Hruby, A. D. Roche, D. Farina, R. Blumer, O. C. Aszmann, Axonal components of nerves innervating the human arm. *Ann. Neurol.* **82**, 396–408 (2017).
10. Y. D. Gu, G. M. Zhang, D. S. Chen, J. G. Yan, X. M. Cheng, L. Chen, Seventh cervical nerve root transfer from the contralateral healthy side for treatment of brachial plexus root avulsion. *J. Hand Surg. Br.* **17**, 518–521 (1992).
11. J. K. Terzis, Z. T. Kokkalis, Selective contralateral C7 transfer in posttraumatic brachial plexus injuries: A report of 56 cases. *Plast. Reconstr. Surg.* **123**, 927–938 (2009).
12. E. F. Willis, K. P. A. MacDonald, Q. H. Nguyen, A. L. Garrido, E. R. Gillespie, S. B. R. Harley, P. F. Bartlett, W. A. Schroder, A. G. Yates, D. C. Anthony, S. Rose-John, M. J. Ruitenberg, J. Vukovic, Repopulating microglia promote brain repair in an IL-6-dependent manner. *Cell* **180**, 833–846.e16 (2020).
13. T. C. Harrison, O. G. Ayling, T. H. Murphy, Distinct cortical circuit mechanisms for complex forelimb movement and motor map topography. *Neuron* **74**, 397–409 (2012).
14. M. Ueno, Y. Nakamura, J. Li, Z. Gu, J. Niehaus, M. Maezawa, S. A. Crone, M. Goulding, M. L. Baccei, Y. Yoshida, Corticospinal circuits from the sensory and motor cortices

differentially regulate skilled movements through distinct spinal interneurons. *Cell Rep.* **23**, 1286–1300.e7 (2018).
15. R. Hira, F. Ohkubo, K. Ozawa, Y. Isomura, K. Kitamura, M. Kano, H. Kasai, M. Matsuzaki, Spatiotemporal dynamics of functional clusters of neurons in the mouse motor cortex during a voluntary movement. *J. Neurosci.* **33**, 1377–1390 (2013).
16. X. Wang, Y. Liu, X. Li, Z. Zhang, H. Yang, Y. Zhang, P. R. Williams, N. S. A. Alwahab, K. Kapur, B. Yu, Y. Zhang, M. Chen, H. Ding, C. R. Gerfen, K. H. Wang, Z. He, Deconstruction of corticospinal circuits for goal-directed motor skills. *Cell* **171**, 440–455.e14 (2017).
17. D. J. Guggenmos, M. Azin, S. Barbay, J. D. Mahnken, C. Dunham, P. Mohseni, R. J. Nudo, Restoration of function after brain damage using a neural prosthesis. *Proc. Natl. Acad. Sci. U.S.A.* **110**, 21177–21182 (2013).
18. R. Hira, F. Ohkubo, Y. R. Tanaka, Y. Masamizu, G. J. Augustine, H. Kasai, M. Matsuzaki, In vivo optogenetic tracing of functional corticocortical connections between motor forelimb areas. *Front Neural Circuits* **7**, 55 (2013).
19. R. Cai, C. Pan, A. Ghasemigharagoz, M. I. Todorov, B. Förstera, S. Zhao, H. S. Bhatia, A. Parra-Damas, L. Mrowka, D. Theodorou, M. Rempfler, A. L. R. Xavier, B. T. Kress, C. Benakis, H. Steinke, S. Liebscher, I. Bechmann, A. Liesz, B. Menze, M. Kerschensteiner, M. Nedergaard, A. Ertürk, Panoptic imaging of transparent mice reveals whole-body neuronal projections and skull-meninges connections. *Nat. Neurosci.* **22**, 317–327 (2019).
20. L. Asboth, L. Friedli, J. Beauparlant, C. Martinez-Gonzalez, S. Anil, E. Rey, L. Baud, G. Pidpruzhnykova, M. A. Anderson, P. Shkorbatova, L. Batti, S. Pagès, J. Kreider, B. L. Schneider, Q. Barraud, G. Courtine, Cortico-reticulo-spinal circuit reorganization enables functional recovery after severe spinal cord contusion. *Nat. Neurosci.* **21**, 576–588 (2018).
21. T. C. Wen, S. Lall, C. Pagnotta, J. Markward, D. Gupta, S. Ratnadurai-Giridharan, J. Bucci, L. Greenwald, M. Klugman, N. J. Hill, J. B. Carmel, Corrigendum: Plasticity in one hemisphere, control from two: Adaptation in descending motor pathways after unilateral corticospinal injury in neonatal rats. *Front Neural Circuits* **12**, 28 (2018).
22. T. A. Jones, Motor compensation and its effects on neural reorganization after stroke. *Nat. Rev. Neurosci.* **18**, 267–280 (2017).
23. T. H. Hutson, C. Kathe, I. Palmisano, K. Bartholdi, A. Hervera, F. de Virgiliis, E. McLachlan, L. Zhou, G. Kong, Q. Barraud, M. C. Danzi, A. Medrano-Fernandez, J. P. Lopez-Atalaya, A. L. Boutillier, S. H. Sinha, A. K. Singh, P. Chaturbedy, L. D. F. Moon, T. K. Kundu, J. L. Bixby, V. P. Lemmon, A. Barco, G. Courtine, S. di Giovanni, Cbp-dependent histone acetylation mediates axon regeneration induced by environmental enrichment in rodent spinal cord injury models. *Sci. Transl. Med.* **11**, eaaw2064 (2019).
24. S. Li, J. J. Overman, D. Katsman, S. V. Kozlov, C. J. Donnelly, J. L. Twiss, R. J. Giger, G. Coppola, D. H. Geschwind, S. T. Carmichael, An age-related sprouting transcriptome provides molecular control of axonal sprouting after stroke. *Nat. Neurosci.* **13**, 1496–1504 (2010).
25. B. Cauli, X. K. Tong, A. Rancillac, N. Serluca, B. Lambolez, J. Rossier, E. Hamel, Cortical GABA interneurons in neurovascular coupling: Relays for subcortical vasoactive pathways. *J. Neurosci.* **24**, 8940–8949 (2004).
26. S. Li, P. Kumar T, S. Joshee, T. Kirschstein, S. Subburaju, J. S. Khalili, J. Kloepper, C. du, A. Elkhal, G. Szabó, R. K. Jain, R. Köhling, A. Vasudevan, Endothelial cell-derived GABA signaling modulates neuronal migration and postnatal behavior. *Cell Res.* **28**, 221–248 (2018).
27. J. C. Wester, V. Mahadevan, C. T. Rhodes, D. Calvigioni, S. Venkatesh, D. Maric, S. Hunt, X. Yuan, Y. Zhang, T. J. Petros, C. J. McBain, Neocortical projection neurons instruct inhibitory interneuron circuit development in a lineage-dependent manner. *Neuron* **102**, 960–975.e6 (2019).
28. A. Bhattacherjee, M. N. Djekidel, R. Chen, W. Chen, L. M. Tuesta, Y. Zhang, Cell type-specific transcriptional programs in mouse prefrontal cortex during adolescence and addiction. *Nat. Commun.* **10**, 4169 (2019).
29. C. Fraser, M. Power, S. Hamdy, J. Rothwell, D. Hobday, I. Hollander, P. Tyrell, A. Hobson, S. Williams, D. Thompson, Driving plasticity in human adult motor cortex is associated with improved motor function after brain injury. *Neuron* **34**, 831–840 (2002).
30. L. L. Edwards, E. M. King, C. M. Buetefisch, M. R. Borich, Putting the "sensory" into sensorimotor control: The role of sensorimotor integration in goal-directed hand movements after stroke. *Front. Integr. Neurosci.* **13**, 16 (2019).
31. F. Pischiutta, E. Micotti, J. R. Hay, I. Marongiu, E. Sammali, D. Tolomeo, G. Vegliante, N. Stocchetti, G. Forloni, M. G. de Simoni, W. Stewart, E. R. Zanier, Single severe traumatic brain injury produces progressive pathology with ongoing contralateral white matter damage one year after injury. *Exp. Neurol.* **300**, 167–178 (2018).
32. Y. Liu, X. Wang, W. Li, Q. Zhang, Y. Li, Z. Zhang, J. Zhu, B. Chen, P. R. Williams, Y. Zhang, B. Yu, X. Gu, Z. He, A sensitized IGF1 treatment restores corticospinal axon-dependent functions. *Neuron* **95**, 817–833.e4 (2017).
33. M. L. Starkey, A. W. Barritt, P. K. Yip, M. Davies, F. P. T. Hamers, S. B. McMahon, E. J. Bradbury, Assessing behavioural function following a pyramidotomy lesion of the corticospinal tract in adult mice. *Exp. Neurol.* **195**, 524–539 (2005).
34. J. Feng, T. Li, M. Lv, S. Kim, J. H. Shin, N. Zhao, Q. Chen, Y. Gong, Y. Sun, Z. Zhao, N. Zhu, J. Cao, W. Fang, B. Chen, S. Zheng, Z. Xu, X. Jin, Y. Shen, Y. Qiu, H. Yin, S. Jiang, J. Li, Y. Ying, L. Chen, Y. Liu, J. Jia, C. Zuo, J. Xu, Y. Gu, W. Xu, Reconstruction of paralyzed arm function in patients with hemiplegia through contralateral seventh cervical nerve cross transfer: A multicenter study and real-world practice guidance. *EClinicalMedicine* **43**, 101258 (2022).
35. T. M. Rotterman, E. T. Akhter, A. R. Lane, K. MacPherson, V. V. García, M. G. Tansey, F. J. Alvarez, Spinal motor circuit synaptic plasticity after peripheral nerve injury depends on microglia activation and a CCR2 mechanism. *J. Neurosci.* **39**, 3412–3433 (2019).
36. H. Yamashita, S. Chen, S. Komagata, R. Hishida, T. Iwasato, S. Itohara, T. Yagi, N. Endo, M. Shibata, K. Shibuki, Restoration of contralateral representation in the mouse somatosensory cortex after crossing nerve transfer. *PLOS ONE* **7**, e35676 (2012).
37. N. Yamawaki, M. G. Raineri Tapies, A. Stults, G. A. Smith, G. M. Shepherd, Circuit organization of the excitatory sensorimotor loop through hand/forelimb S1 and M1. *eLife* **10**, e66836 (2021).
38. A. Ghosh, F. Haiss, E. Sydekum, R. Schneider, M. Gullo, M. T. Wyss, T. Mueggler, C. Baltes, M. Rudin, B. Weber, M. E. Schwab, Rewiring of hindlimb corticospinal neurons after spinal cord injury. *Nat. Neurosci.* **13**, 97–104 (2010).
39. B. M. Hooks, T. Mao, D. A. Gutnisky, N. Yamawaki, K. Svoboda, G. M. G. Shepherd, Organization of cortical and thalamic input to pyramidal neurons in mouse motor cortex. *J. Neurosci.* **33**, 748–760 (2013).
40. M. Quiquempoix, S. L. Fayad, K. Boutourlinsky, N. Leresche, R. C. Lambert, T. Bessaih, Layer 2/3 pyramidal neurons control the gain of cortical output. *Cell Rep.* **24**, 2799–2807. e4 (2018).
41. A. S. Wahl, W. Omlor, J. C. Rubio, J. L. Chen, H. Zheng, A. Schröter, M. Gullo, O. Weinmann, K. Kobayashi, F. Helmchen, B. Ommer, M. E. Schwab, Neuronal repair. Asynchronous therapy restores motor control by rewiring of the rat corticospinal tract after stroke. *Science* **344**, 1250–1255 (2014).
42. Y. Liu, A. Latremoliere, X. Li, Z. Zhang, M. Chen, X. Wang, C. Fang, J. Zhu, C. Alexandre, Z. Gao, B. Chen, X. Ding, J. Y. Zhou, Y. Zhang, C. Chen, K. H. Wang, C. J. Woolf, Z. He, Touch and tactile neuropathic pain sensitivity are set by corticospinal projections. *Nature* **561**, 547–550 (2018).
43. S. K. Karadimas, K. Satkunendrarajah, A. M. Laliberte, D. Ringuette, I. Weisspapir, L. Li, S. Gosgnach, M. G. Fehlings, Sensory cortical control of movement. *Nat. Neurosci.* **23**, 75–84 (2020).
44. D. T. Bundy, E. C. Leuthardt, The cortical physiology of ipsilateral limb movements. *Trends Neurosci.* **42**, 825–839 (2019).
45. T. H. Murphy, D. Corbett, Plasticity during stroke recovery: From synapse to behaviour. *Nat. Rev. Neurosci.* **10**, 861–872 (2009).
46. A. Biasiucci, R. Leeb, I. Iturrate, S. Perdikis, A. al-Khodairy, T. Corbet, A. Schnider, T. Schmidlin, H. Zhang, M. Bassolino, D. Viceic, P. Vuadens, A. G. Guggisberg, J. d. R. Millán, Brain-actuated functional electrical stimulation elicits lasting arm motor recovery after stroke. *Nat. Commun.* **9**, 2421 (2018).
47. U. Chaudhary, N. Birbaumer, A. Ramos-Murguialday, Brain-computer interfaces for communication and rehabilitation. *Nat. Rev. Neurol.* **12**, 513–525 (2016).
48. P. D. Ganzer, S. C. Colachis IV, M. A. Schwemmer, D. A. Friedenberg, C. F. Dunlap, C. E. Swiftney, A. F. Jacobowitz, D. J. Weber, M. A. Bockbrader, G. Sharma, Restoring the sense of touch using a sensorimotor demultiplexing neural interface. *Cell* **181**, 763–773.e12 (2020).
49. L. M. Alonso-Valerdi, R. A. Salido-Ruiz, R. A. Ramirez-Mendoza, Motor imagery based brain-computer interfaces: An emerging technology to rehabilitate motor deficits. *Neuropsychologia* **79**, 354–363 (2015).
50. A. Takeoka, I. Vollenweider, G. Courtine, S. Arber, Muscle spindle feedback directs locomotor recovery and circuit reorganization after spinal cord injury. *Cell* **159**, 1626–1639 (2014).
51. M. X. Zheng, X. Y. Hua, S. Jiang, Y. Q. Qiu, Y. D. Shen, W. D. Xu, Contralateral peripheral neurotization for a hemiplegic hindlimb after central neurological injury. *J. Neurosurg.* **128**, 304–311 (2018).
52. P. A. Walker, S. S. Bedi, S. K. Shah, F. Jimenez, H. Xue, J. A. Hamilton, P. Smith, C. P. Thomas, R. W. Mays, S. Pati, C. S. Cox Jr., Intravenous multipotent adult progenitor cell therapy after traumatic brain injury: Modulation of the resident microglia population. *J. Neuroinflammation* **9**, 228 (2012).
53. W. Gao, F. Li, Z. Zhou, X. Xu, Y. Wu, S. Zhou, D. Yin, D. Sun, J. Xiong, R. Jiang, J. Zhang, IL-2/anti-IL-2 complex attenuates inflammation and BBB disruption in mice subjected to traumatic brain injury. *Front. Neurol.* **8**, 281 (2017).
54. X. Ye, Y. D. Shen, J. T. Feng, F. Wang, Z. R. Gao, G. W. Lei, A. P. Yu, C. P. Wang, C. M. Liang, W. D. Xu, A novel mouse model of contralateral C7 transfer via the pretracheal route: A feasibility study. *J. Neurosci. Methods* **328**, 108445 (2019).
55. Z. Gao, G. Lei, Z. Pang, Y. Chen, S. Zhu, K. Huang, W. Lin, Y. Shen, W. Xu, A mouse model of direct anastomosis via the prespinal route for crossing nerve transfer surgery. *JoVE* e63051 (2021).

56. M. Cheah, J. W. Fawcett, M. R. Andrews, Dorsal root ganglion injection and dorsal root crush injury as a model for sensory axon regeneration. *J. Vis. Exp.* 55535 (2017).
57. Z. R. Gao, W.-Z. Chen, M.-Z. Liu, X.-J. Chen, L. Wan, X.-Y. Zhang, L. Yuan, J.-K. Lin, M. Wang, L. Zhou, X.-H. Xu, Y.-G. Sun, Tac1-expressing neurons in the periaqueductal gray facilitate the itch-scratching cycle via descending regulation. *Neuron* **101**, 45–59.e9 (2019).
58. E. C. Meyers, N. Kasliwal, B. R. Solorzano, E. Lai, G. Bendale, A. Berry, P. D. Ganzer, M. Romero-Ortega, R. L. Rennaker II, M. P. Kilgard, S. A. Hays, Enhancing plasticity in central networks improves motor and sensory recovery after nerve damage. *Nat. Commun.* **10**, 5782 (2019).
59. Y. C. Chuang, C. H. Lee, W. H. Sun, C. C. Chen, Involvement of advillin in somatosensory neuron subtype-specific axon regeneration and neuropathic pain. *Proc. Natl. Acad. Sci. U.S.A.* **115**, E8557–E8566 (2018).
60. D. Liu, W. Li, C. Ma, W. Zheng, Y. Yao, C. F. Tso, P. Zhong, X. Chen, J. H. Song, W. Choi, S. B. Paik, H. Han, Y. Dan, A common hub for sleep and motor control in the substantia nigra. *Science* **367**, 440–445 (2020).
61. P. Bankhead, M. B. Loughrey, J. A. Fernández, Y. Dombrowski, D. G. McArt, P. D. Dunne, S. McQuaid, R. T. Gray, L. J. Murray, H. G. Coleman, J. A. James, M. Salto-Tellez, P. W. Hamilton, QuPath: Open source software for digital pathology image analysis. *Sci. Rep.* **7**, 16878 (2017).
62. H. Dana, T. W. Chen, A. Hu, B. C. Shields, C. Guo, L. L. Looger, D. S. Kim, K. Svoboda, Thy1-GCaMP6 transgenic mice for neuronal population imaging in vivo. *PLOS ONE* **9**, e108697 (2014).
63. M. S. Esposito, P. Capelli, S. Arber, Brainstem nucleus MdV mediates skilled forelimb motor tasks. *Nature* **508**, 351–356 (2014).
64. J. J. Overman, A. N. Clarkson, I. B. Wanner, W. T. Overman, I. Eckstein, J. L. Maguire, I. D. Dinov, A. W. Toga, S. T. Carmichael, A role for ephrin-A5 in axonal sprouting, recovery, and activity-dependent plasticity after stroke. *Proc. Natl. Acad. Sci. U.S.A.* **109**, E2230–E2239 (2012).
65. A. N. Clarkson, J. J. Overman, S. Zhong, R. Mueller, G. Lynch, S. T. Carmichael, AMPA receptor-induced local brain-derived neurotrophic factor signaling mediates motor recovery after stroke. *J. Neurosci.* **31**, 3766–3775 (2011).
66. O. Steward, K. M. Yee, M. Metcalfe, R. Willenberg, J. Luo, R. Azevedo, J. H. Martin-Thompson, S. P. Gandhi, Rostro-caudal specificity of corticospinal tract projections in mice. *Cereb. Cortex* **31**, 2322–2344 (2021).
67. R. Satija, J. A. Farrell, D. Gennert, A. F. Schier, A. Regev, Spatial reconstruction of single-cell gene expression data. *Nat. Biotechnol.* **33**, 495–502 (2015).
68. T. Stuart, A. Butler, P. Hoffman, C. Hafemeister, E. Papalexi, W. M. Mauck III, Y. Hao, M. Stoeckius, P. Smibert, R. Satija, Comprehensive integration of single-cell data. *Cell* **177**, 1888–1902.e21 (2019).
69. G. C. Linderman, M. Rachh, J. G. Hoskins, S. Steinerberger, Y. Kluger, Fast interpolation-based t-SNE for improved visualization of single-cell RNA-seq data. *Nat. Methods* **16**, 243–245 (2019).
70. D. Aran, A. P. Looney, L. Liu, E. Wu, V. Fong, A. Hsu, S. Chak, R. P. Naikawadi, P. J. Wolters, A. R. Abate, A. J. Butte, M. Bhattacharya, Reference-based analysis of lung single-cell sequencing reveals a transitional profibrotic macrophage. *Nat. Immunol.* **20**, 163–172 (2019).
71. K. A. Tennant, D. A. L. Adkins, N. A. Donlan, A. L. Asay, N. Thomas, J. A. Kleim, T. A. Jones, The organization of the forelimb representation of the C57BL/6 mouse motor cortex as defined by intracortical microstimulation and cytoarchitecture. *Cereb. Cortex* **21**, 865–876 (2011).

Acknowledgments: We thank Y.-F. Zhang, Y.-T. Yuan, Y.-H. Shi, C.-P. Wang, and Y. Dong for technical support; and Y.-H. Cui, D.-Q. Liu, H.-B. Zhou, Y. Li, and all members of laboratory for discussions. We also thank the team of Lunion Data for providing custom software development and technical support on data processing. **Funding:** This work was supported by the National Science Foundation of China (81830063, 81873766, 81902296, 82071406, and 82021002), CAMS Innovation Fund for Medical Sciences (2019-I2M-5-007), Shanghai Natural Science Foundation (20XD1420700 and 22ZR1479000), and National Postdoctoral Program for Innovative Talents (BX20190075). **Author contributions:** W.X., Y.S., and Z.G. designed the project and experiments. Z.G. and Z.P. performed most experiments and data analysis. G.L., Y.C., S.Z., W.L., and Z.P. conducted behavioral experiments. Z.G. and Z.P. wrote the manuscript. Y.S., G.L., Z.C., Y.C., Z.P., S.Z., and W.L. performed the mouse models. Z.P. conducted histological and biochemical experiments. Y.C. conducted electrophysiological experiments. Z.C. and W.L. conducted viral preparation. Z.Q. and Y.W. interpreted the data. We shared the data with all authors who contributed to the analysis and interpretation of the data and to the design of the experiments. **Competing interests:** The authors declare that they have no competing interests. **Data and materials availability:** All data needed to evaluate the conclusions in the paper are present in the paper and/or the Supplementary Materials. Codes and data for reproducing main simulations are freely available at https://datadryad.org/stash/share/-OD1h4ATO8mn9U7c75G38CWNmJ0x87l-esBXTnswBHo.

Submitted 7 December 2021
Accepted 18 July 2022
Published 31 August 2022
10.1126/sciadv.abn5899